

*Boundary layer recovery and precipitation
symmetrization preceding rapid
intensification of tropical cyclones under
shear*

Article

Accepted Version

Chen, X., Gu, J.-F. ORCID: <https://orcid.org/0000-0002-7752-4553>, Zhang, J. A., Marks, F. D., Rogers, R. F. and Cione, J. J. (2021) Boundary layer recovery and precipitation symmetrization preceding rapid intensification of tropical cyclones under shear. *Journal of the Atmospheric Sciences*, 78 (5). pp. 1523-1544. ISSN 0022-4928 doi: 10.1175/jas-d-20-0252.1 Available at <https://centaur.reading.ac.uk/96833/>

It is advisable to refer to the publisher's version if you intend to cite from the work. See [Guidance on citing](#).

To link to this article DOI: <http://dx.doi.org/10.1175/jas-d-20-0252.1>

Publisher: American Meteorological Society

All outputs in CentAUR are protected by Intellectual Property Rights law, including copyright law. Copyright and IPR is retained by the creators or other copyright holders. Terms and conditions for use of this material are defined in the [End User Agreement](#).

www.reading.ac.uk/centaur

CentAUR

Central Archive at the University of Reading

Reading's research outputs online



1
2
3
4 **Boundary Layer Recovery and Precipitation Symmetrization Preceding Rapid**
5 **Intensification of Tropical Cyclones under Shear**

6
7 Xiaomin Chen^{1*}, Jian-Feng Gu², Jun A. Zhang^{1, 3}, Frank D. Marks¹, Robert F. Rogers¹, and
8 Joseph J. Cione¹

9 ¹NOAA/AOML Hurricane Research Division, Miami, FL, USA

10 ²Department of Meteorology, University of Reading, Reading, UK

11 ³University of Miami, Cooperative Institute for Marine and Atmospheric Studies, Miami, FL,
12 USA

13
14
15
16
17 Submitted to *Journal of the Atmospheric Sciences*

18
19
20 Revised by February 22, 2021
21

* Corresponding author: Dr. Xiaomin Chen (xiaomin.chen@noaa.gov)

Early Online Release: This preliminary version has been accepted for publication in *Journal of the Atmospheric Sciences*, may be fully cited, and has been assigned DOI 10.1175/JAS-D-20-0252.1. The final typeset copyedited article will replace the EOR at the above DOI when it is published.

22 **Abstract**

23 This study investigates the precipitation symmetrization preceding rapid intensification (RI)
24 of tropical cyclones (TCs) experiencing vertical wind shear by analyzing numerical simulations
25 of Typhoon Mujigae (2015) with warm (CTL) and relatively cool (S1) sea surface temperatures
26 (SSTs). A novel finding is that precipitation symmetrization is maintained by the continuous
27 development of deep convection along the inward flank of a convective precipitation shield
28 (CPS), especially in the downwind part. Beneath the CPS, downdrafts flush the boundary layer
29 with low-entropy parcels. These low-entropy parcels do not necessarily weaken the TCs; instead,
30 they are “recycled” in the TC circulation, gradually recovered by positive enthalpy fluxes, and
31 develop into convection during their propagation toward a downshear convergence zone. Along-
32 trajectory vertical momentum budget analyses reveal the predominant role of buoyancy
33 acceleration in the convective development in both experiments. The boundary layer recovery is
34 more efficient for warmer SST, and the stronger buoyancy acceleration accounts for the higher
35 probability of these parcels developing into deep convection in the downwind part of the CPS,
36 which helps maintain the precipitation symmetrization in CTL. In contrast, less efficient
37 boundary layer recovery and less upshear deep convection hinder the precipitation
38 symmetrization in S1. These findings highlight the key role of boundary layer recovery in
39 regulating the precipitation symmetrization and upshear deep convection, which further accounts
40 for an earlier RI onset timing of the CTL TC. The inward rebuilding pathway also illuminates
41 why deep convection is preferentially located inside the radius of maximum wind of sheared TCs
42 undergoing RI.

43 **1. Introduction**

44 Accurate forecasts of rapid intensification (RI) of tropical cyclones (TCs) remain a
45 challenging task (DeMaria et al. 2014), especially under moderate vertical wind shear (VWS)
46 (Bhatia and Nolan 2013). Whether and when a TC is going to undergo RI under moderate VWS
47 depends crucially on the other environmental factors including sea surface temperature and
48 environment humidity (Tao and Zhang 2014). This forecast challenge becomes even more acute
49 for prelandfall RI forecasts. One recent example in point is Hurricane Michael (2018), which
50 underwent an unexpected prelandfall RI¹ under moderate VWS and became a category-5
51 hurricane near landfall.

52 In the presence of VWS, dry TC-like vortices are usually vertically tilted (Jones 1995,
53 2004). When coupled with moist processes, the balanced mesoscale lifting associated with the
54 tilted vortex organizes a convective precipitation shield (CPS) in the downtilt side (e.g., Wang
55 and Holland 1996; Corbosiero and Molinari 2002; Reasor et al. 2013; Gu et al. 2019).
56 Observational and modeling studies of early-stage TCs² under moderate VWS indicate a
57 common feature before RI onset: as the midlevel TC vortex precesses from the downshear-left to
58 upshear and the TC vortex becomes nearly vertically aligned, the CPS also propagates into the
59 upshear flank and spirals inward toward the formation of an incipient eyewall (e.g., Rappin and
60 Nolan 2012; Zhang and Tao 2013; Alvey et al. 2015; Rogers et al. 2016; Chen et al. 2017;
61 Leighton et al. 2018; Rios-Berrios et al. 2018; Ryglicki et al. 2018). This process is also termed
62 precipitation symmetrization. The radius of maximum wind (RMW) contracts inward
63 significantly during the vortex alignment and precipitation symmetrization, as documented in

¹ The prelandfall RI means that the RI occurs within 1-2 days of landfall and the RI can last to the landfall time.

² Early-stage TCs include the tropical depressions, tropical storms, and Category-1 hurricanes.

64 previous studies (e.g., Judt and Chen 2016; Chen et al. 2018a, b; Miyamoto and Nolan 2018;
65 Tang et al. 2019). The coupled inner-core structural and precipitation evolution preceding RI
66 onset for TCs in shear indicates the necessity to examine these processes in an integrated
67 framework before proposing a theoretical explanation for RI onset in shear.

68 The contribution of the deep convection in the CPS to vortex alignment has been examined
69 in previous studies, and two different pathways have been proposed, either through the
70 downshear reformation that involves a newly formed center (Molinari et al. 2004; Molinari et al.
71 2006; Nguyen and Molinari 2015; Chen et al. 2018b; Rogers et al. 2020) or through an inner-
72 core vorticity “restructuring” process (Rios-Berrios et al. 2018; Miyamoto and Nolan 2018;
73 Shimada and Horinouchi 2018). Both pathways involve sustained deep convection in the
74 azimuthally-propagating CPS and continuous merger of convectively-induced vorticity
75 anomalies. In an analytical study using a shallow-water model, Schecter (2020) demonstrated
76 that the two different pathways mentioned above can be explained by the relative strength
77 between the velocity-convergence generated by the mass sink on the downshear side (cf. the
78 downshear convergence zone in Chen et al. 2018b) and a critical value that is determined by the
79 horizontal scale of the mass sink as well as the absolute value of the drift velocity of the mass
80 sink relative to the background cyclonic flow.

81 The linkage between the precipitation symmetrization and RMW contraction was also
82 examined in a modeling study (Chen et al. 2018a). By performing a set of numerical simulations
83 for Typhoon Mujigae (2015) over various sea surface temperatures (SSTs), Chen et al. (2018a)
84 found that TCs over different SSTs all undergo vertical alignment and precipitation
85 symmetrization before RI onset. However, over warmer SST TCs exhibit a higher degree of
86 precipitation symmetry, and the RMW contraction and RI occur much earlier. Diagnoses using

87 the Sawyer-Eliassen equation indicate that the stronger diabatic heating due to more midlevel
88 and deep convection within the inner core (also within the CPS) contributes to the earlier RMW
89 contraction of the TCs over warmer SST. These results are consistent with earlier analytical
90 analyses invoking balanced dynamics in that diabatic heating near/inside of the RMW benefits
91 the RMW contraction and TC intensification (Schubert and Hack 1982; Pendergrass and
92 Willoughby 2009).

93 Given the pivotal role of deep convection in both vortex alignment and RMW contraction,
94 understanding the mechanisms that maintain the deep convection in the CPS during precipitation
95 symmetrization is key. Convective downdrafts can bring low-entropy air parcels into the
96 boundary layer and cool the inflow layer (Tang and Emanuel 2010; Riemer et al. 2010; Zhang et
97 al. 2013; Gu et al. 2015; Wadler et al. 2018b; Chen et al. 2019), i.e., the low-level ventilation,
98 which is argued as the most detrimental pathway of VWS to weaken a TC (Riemer et al. 2010,
99 2013). The boundary layer recovery of these downdraft-cooled parcels by the surface enthalpy
100 fluxes is argued as the key to compensate for the low-level ventilation and impacts the
101 subsequent TC intensity change (Powell 1990; Tang and Emanuel 2012; Molinari et al. 2013;
102 Zhang et al. 2017b; Zhang and Rogers 2019; Nguyen et al. 2019). However, the linkage between
103 the boundary layer recovery and convective development in sheared TCs remains elusive: recent
104 idealized simulations with the same SST attribute convective initiation in the azimuthally-
105 propagating CPS before RI onset to dynamical forcing, rather than buoyancy forcing (Gu et al.
106 2019).

107 As a follow-up of Chen et al. (2018a), this study will further examine the numerical
108 simulation dataset for Typhoon Mujigae (2015) over various SSTs. It is hypothesized that the
109 boundary layer recovery is more effective under warmer SST conditions, and a comparison of

110 two representative experiments with warm and relatively cool SSTs provides a unique
111 opportunity to gain insight into the role of boundary layer recovery in governing the distribution
112 of deep convection within the TC inner core, which is the key to further understand the
113 relationship between precipitation symmetrization, RMW contraction, and RI onset for sheared
114 TCs. The specific scientific questions to be addressed in this study include:

- 115 1) Before RI onset, how is the CPS organized and maintained during precipitation
116 symmetrization under VWS?
- 117 2) What is the role of boundary layer recovery in the convective development and
118 precipitation symmetrization?
- 119 3) What is the relative importance between dynamical and buoyancy forcing in the
120 convective development?

121 The remainder of this paper is organized as follows. Section 2 describes the methods and
122 simulation datasets used in this study. Section 3 provides an overview of the vortex intensity and
123 structural change, and precipitation evolution prior to the RI onset in warm and relatively cool
124 SST experiments. Section 4 compares the organization of the CPS during precipitation
125 symmetrization in the two experiments. The role of boundary layer recovery in the convective
126 development and precipitation symmetrization is discussed in section 5. Additional discussion
127 and concluding remarks are given in sections 6 and 7, respectively.

128 **2. Data and Methods**

129 Following Chen et al. (2018a), the same two representative WRF-ARW experiments of
130 Typhoon Mujigae (2015) with warm (CTL) and relatively cool (S1) SSTs are compared in this
131 study. The model setup for these two experiments is the same except for the initial SST. In CTL,
132 the SST is set as the initial condition at 0000 UTC 2 October, while in S1 the SST is set as the

133 climatological monthly-mean state (MMSST) averaged from 1990 to 2013. The MMSST
134 averaged in the South China Sea is 28.6°C, 1°C cooler than that in CTL. For simplicity, the
135 ocean coupling is not included and the SST is not updated during the simulation in these
136 experiments. The horizontal resolution of the triple-nested domains is 12, 4, and 1.33 km,
137 respectively. The outermost domain is static and the inner two domains move with the simulated
138 TC. All three domains contain 51 sigma levels with the top level at 50 hPa. The CTL simulation
139 successfully captures the track, prelandfall RI, and storm structure evolution. In comparison, the
140 RI onset timing lags by 13 h in the S1 experiment and the intensification rate is much weaker.
141 For more details of model setup, verification, and differences in the two experiments, we refer
142 interested readers to Chen et al. (2018a).

143 The objective partitioning method proposed by Rogers (2010) is adopted to separate the
144 convective, stratiform, and other (typically flanking the stratiform) type precipitation. This
145 method uses reflectivity criteria at 0.9 and 3 km heights and a threshold of vertical velocity
146 averaged between 0.9 and 2.1 km (i.e., $>0.5 \text{ m s}^{-1}$) to identify convective points. If one grid point
147 is not flagged as a convective point and 3-km reflectivity is $>20 \text{ dBZ}$, it is flagged as stratiform
148 precipitation [for more details, see Rogers (2010)]. Then, based on the height of cloud top,
149 indicated by 20-dBZ echo top, the convective region is further divided into shallow ($< 4 \text{ km}$),
150 midlevel (4-8 km), and deep ($>8 \text{ km}$) convection following Fritz et al. (2016). We also pay
151 attention to one type of extreme deep convection, namely convective bursts (CBs) and adopt the
152 definition proposed by Rogers (2010). A CB is defined as a grid point where the layer-averaged
153 vertical velocity within the 300–700-hPa layer exceeds 5 m s^{-1} .

154 A forward trajectory analysis is performed in section 5 to investigate the boundary layer
155 recovery of the downdraft-cooled parcels. To compute the trajectory of air parcels ending in

156 rapidly changing convection, output from the innermost domain is saved every 1 min. The
157 parcels to be tracked are selected near the TC center and beneath the vortex-tilt-related CPS, and
158 their trajectories over the analysis period do not cross the boundary of the innermost moving
159 nest. The predictor-corrector technique is used for the trajectory calculation, following
160 Onderlinde and Nolan (2016). The essence of this technique is to use the wind information at the
161 predicted midpoint to advect the parcel at the initial location for a full-time step. The predicted
162 midpoint is determined by advecting the parcel from the initial location by a half time step using
163 the wind information at the initial location. The time step selected is 30s, since a higher temporal
164 resolution produces similar results.

165 The TC center at a given pressure level is defined as the geopotential height centroid (Chen
166 et al. 2018b), which is skillful at locating the TC center for weak storms (Nguyen et al. 2014).
167 Vortex tilt is calculated as the distance between the TC centers at 450 hPa and 850 hPa pressure
168 levels.

169 **3. Overview of vortex intensity and structural change prior to RI onset**

170 Typhoon Mujigae underwent RI over the warm water in the South China Sea under
171 moderate VWS. The magnitude of 200-850 hPa VWS remained 7-8 m s⁻¹ before RI onset³ (i.e.,
172 0000 UTC 3 October). Note that the 200–850-hPa VWS is calculated for the area between 200
173 and 800 km from the surface TC center. The VWS subsequently decreased to 4-5 m s⁻¹ during
174 the early RI period and then increased to 7-9 m s⁻¹ near the end of RI, which was followed by the
175 landfall near 0600 UTC 4 October. Both simulations have similar VWS evolution to
176 observations. The CTL TC successfully reproduces the intensity evolution, and its RI lasts from

³ RI onset in this study is defined as the time when the increase in 10-m maximum wind speed (VMAX) exceeds 15 m s⁻¹ in the subsequent 24 h or shorter period, if the RI duration is less than 1 day. An additional requirement is that the VMAX should increase in the first 6 h of the subsequent 24-h or shorter period.

177 0000 UTC 3 October to 0300 UTC 4 October (Fig. 1a). In comparison, the RI onset of the S1 TC
178 is delayed by 13 h. The RI duration of the S1 TC is ~14h, as the maximum surface wind
179 increases from 29 m s⁻¹ at 1300 UTC 3 October to 46 m s⁻¹ at 0300 UTC 4 October.

180 In addition to the similar evolution of VWS in the two experiments, the CTL and S1 TCs
181 undergo similar vertical alignment prior to RI onset, as the midlevel vortex gradually precesses
182 from the downshear-left quadrant to upshear, and the magnitude of the 400-850 hPa TC vortex
183 tilt decreases with time (Fig. 1b). However, the different RI onset timing between the two TCs
184 suggests vertical alignment, albeit necessary, is not a sufficient RI indicator under moderate
185 VWS. Instead, RI onset in both experiments is effectively indicated when the RMW contraction
186 (Fig. 1d) reaches a certain threshold measured in terms of the local Rossby number at 10-m
187 height ($R_o > 12$, Fig. 1c). The local Rossby number is defined as $R_o = v_m / (r_m f)$, where v_m is
188 the maximum azimuthal mean tangential wind at 10-m height, r_m represents the RMW, and f
189 represents the Coriolis parameter at the TC center. Of note, the R_o threshold (i.e., $R_o > 12$)
190 cannot be overgeneralized beyond this case, which is latitude dependent based on its definition.
191 Additionally, the value of R_o at RI onset varies by changing the size and intensity of the initial
192 vortex, translational speed, and VWS magnitude (Miyamoto and Nolan 2018). Nonetheless, this
193 metric shows that the CTL TC contracts much earlier and its RI starts much earlier too.

194 Figure 2 shows three snapshots of the simulated radar reflectivity and background
195 horizontal convergence at 1.5-km height for the CTL and S1 experiments. Concurrent with
196 vertical alignment, both TCs undergo precipitation symmetrization before RI onset. The
197 background horizontal convergence is computed with the coarser data resolution of 0.5° × 0.5°
198 that is interpolated from the outermost model domain with a horizontal resolution of 12 km,
199 following Chen et al. (2018b). A mesoscale convergence zone exists in the downshear quadrants

200 of both TCs, which is consistent with the findings in the simulated Typhoon Vicente (2012)
201 (Chen et al. 2018b). The formation of the downshear convergence zone can be explained by the
202 differential vorticity advection by VWS, which induces mesoscale lifting and low-level
203 convergence in the downshear side (Bender 1997; Bracken and Bosart 2000). The convergence
204 zone remains in the downshear side during precipitation symmetrization.

205 **4. Inward rebuilding of CPS during precipitation symmetrization**

206 In this section, we mainly focus on the comparison between CTL and S1 experiments over
207 the 12-h period preceding the RI onset of the CTL TC (i.e., 1200 UTC 2 October–0000 UTC 3
208 October) following Chen et al. (2018a). This is the period when the RMW evolution differs
209 between the two experiments (Fig. 1d), which further impacts the RI onset timing (Fig. 1a).

210 Figures 3a-d show the location of deep convection and CBs within $r = 100$ km in three
211 consecutive 3-h periods at a 10-min interval after 1200 UTC 2 October. In both TCs, deep
212 convection propagates azimuthally from downshear to upshear and meanwhile radially inward
213 toward the TC center over the three periods. The evolution of CBs location over the same
214 periods exhibits similar features in CTL, while the radially inward shift of CBs location is less
215 notable in S1. In this study, *we define the inward rebuilding of the CPS as deep convection*
216 *continuously develops at the inward flank and downwind part of the CPS during precipitation*
217 *symmetrization*. The inward rebuilding process in these two experiments is a reminiscence of the
218 “inward progression” of cloud-to-ground lightning clusters from large radii downshear to smaller
219 radii upshear in RI TCs under moderate VWS (e.g., Molinari et al. 2004; Molinari and Vollaro
220 2010; Stevenson et al. 2014; Zawislak et al. 2016). The inward rebuilding is more notable in
221 CTL, and the CTL TC has much more (1091) grid points of deep convection within the inner-
222 core region (i.e., $r = 60$ km), particularly in the upshear side (Figs. 3a-b and 3e). The CTL TC

223 also has 90 more CBs within the inner core (Fig. 3f), and the difference in the number of CBs
224 between the two TCs is most prominent in the downshear-left quadrant. Nevertheless, the CTL
225 TC has slightly more CBs in the upshear-left quadrant (see Figs. 3c-d and 3f). The difference in
226 the deep convection or CBs in the upshear-left quadrant between the two experiments is
227 consistent with previous observational studies that found deep convection in the upshear-left
228 quadrant is key to determining subsequent intensity change (e.g., Wadler et al. 2018a).

229 An examination of the animation of radar reflectivity at the lowest model level indicates
230 that the newly-developed deep convection related to inward rebuilding are mostly initiate in the
231 downshear-left quadrant inside the RMW and mature along their path toward the downshear
232 convergence zone (see the supplemental movie). Figure 4 presents two examples for the CTL
233 and S1 TCs. In the CTL TC, a 40-50-km long spiral rainband (circled by a thick dashed line) is
234 visible in the downshear-right quadrant at 1710 UTC 2 October (Figs. 4a-b). Of note, this spiral
235 rainband is only visible below the lowest 1.5 km at this moment (not shown), suggesting that it
236 remains in the boundary layer. This rainband gradually develops above the boundary layer and
237 matures (>55 dBZ) during the propagation from the downshear-left to upshear-left quadrant
238 (Figs. 4c-f). The 40-50-km long spiral rainband then becomes the leading edge of the
239 azimuthally propagating CPS as preexisting convection weakens due to its own lifecycle,
240 resulting in an inward rebuilding event. Figures 4g-l show a similar phenomenon occurring over
241 a later period for the S1 TC, i.e., from 1920 UTC 2 October to 2030 UTC 2 October. A notable
242 difference is that the newly-developed spiral rainband in the S1 TC is much weaker than that of
243 the CTL TC in terms of the radar reflectivity. Thus, the convective activity at the downwind part
244 of the CPS in S1 is weaker than that in CTL after this inward rebuilding event (Figs. 4k-l).

245 Figure 5 further compares the composite vertical structure of the newly-developed deep
246 convection between the CTL and S1 TCs over the period of inward rebuilding (see Fig. 4).
247 Dashed lines in Figs. 5a-b mark the locations of the vertical slices in Figs. 5c-f. At $r = 50$ km, the
248 maximum microphysics diabatic heating of the discrete convective tower within the 40-50 km
249 long spiral rainband in CTL exceeds 40 K h^{-1} and the top of the strong diabatic heating ($>40 \text{ K h}^{-1}$)
250 extends to 11 km height (Fig. 5c), indicating that the newly-developed convection (Fig. 5a) is
251 evolving toward its mature stage during its propagation toward the upshear-left quadrant (see
252 Figs. 4d-f). In comparison, the strong diabatic heating ($>40 \text{ K h}^{-1}$) of the newly-developed deep
253 convection in S1 is vertically confined in the 5-8 km layer at $r = \sim 58$ km. The region of larger
254 value of absolute vorticity ($>0.5 \times 10^{-3} \text{ s}^{-1}$) outside of $r = 40$ km in S1 is ~ 4 km shallower than that
255 in CTL (Figs. 5c-d).

256 The composite storm-relative streamlines in Figs. 5e-f indicate two sources of convective
257 updrafts for the matured newly-developed deep convection within $r = 60$ km (Figs. 5e-f). The
258 first source comes from the radial inflow jet ($\theta_e < 354 \text{ K}$) that descends from the freezing level
259 into the boundary layer, pass through the high-entropy ($\theta_e > 358 \text{ K}$) central area within $r = 40$ km,
260 and then becomes outflow above the boundary layer. The inflow to outflow transition is
261 indicative of supergradient wind. The second source is directly traced back to the “eye” region
262 within the lowest 2 km, which is closely related to the inward rebuilding process. Of note, the
263 incipient eyewall with a clear eye appears 2 hours later than the composite period (e.g., Fig. 2c).
264 A comparison of the red streamline in Figs. 5e-f demonstrates that the maximum height related
265 to the second source of convective updrafts differs between the two experiments, as convective
266 updrafts in CTL vertically extend to ~ 17 km height, 5 km taller than the updrafts in S1. These
267 findings in Fig. 5 again suggest that the discrepancies in the strength of newly-developed deep

268 convection inside of the RMW affect the convective activity at the downwind part of the
269 azimuthally propagating CPS.

270 To systematically examine the outward propagation of newly-formed deep convection
271 inside the RMW, Figure 6 shows the evolution of radar reflectivity azimuthally averaged within
272 the downshear-right and downshear-left quadrants below 500-m height in CTL and S1. We only
273 select the downshear quadrants, given that the newly-developed convection typically become
274 visible in the boundary layer of the downshear-left quadrant and convection at the smaller radii
275 in upshear-left may mask the signal of outward propagation of newly-formed deep convection
276 toward the RMW (cf. Fig. 4). This averaging method can capture the distinct inward rebuilding
277 events in which the newly-developed deep convection projects significantly onto the azimuthal
278 mean. Figure 6 presents five and four visually trackable inward rebuilding events over the 12-h
279 period before 0000 UTC 3 October for the CTL and S1 TCs, respectively. The S1 TC undergoes
280 a notable inward rebuilding over 1600-1630 UTC (i.e., the event 1), with the maximum radar
281 reflectivity comparable to that of the inward rebuilding events of the CTL TC. Nevertheless, the
282 strength of outward propagating convection in terms of radar reflectivity is weaker in S1 than
283 that in CTL on average. The outward propagation of the circled spiral rainband shown in Figs.
284 4a-f and Figs. 4g-l corresponds to the event 3 in Fig. 6a and Fig. 6b, respectively.

285 Figures 7a-b further assess the impact of inward rebuilding on precipitation symmetrization
286 and show a time-azimuthal plot of the radar reflectivity averaged within the 20-50 km radii and
287 within the 0-500 m layer for the CTL and S1 TCs, respectively. We select the annulus within the
288 initial RMW (i.e., 60 km) to better illustrate the inward rebuilding of the CPS during
289 precipitation symmetrization. The CPS in CTL spans a broader azimuthal coverage and generally
290 exhibits a more vigorous convective activity in terms of radar reflectivity than the CPS in S1

291 over the 12-h period, and the latter is consistent with Fig. 6. Precipitation symmetrization in CTL
292 is sustained with more vigorous convection over the 12-h period; however, precipitation
293 symmetrization in S1 is only notable when the convective activity is most vigorous over 1600-
294 1830 UTC (see the reflectivity maximum in Fig. 7b). These findings demonstrate that
295 precipitation symmetrization is closely related to the strength of the outward propagating newly-
296 developed deep convection inside the RMW (see also Figs. 4-6). Additionally, the relatively
297 weak echo (10-25 dBZ) in the right-of-shear quadrants of the CTL TC is related to stratiform
298 precipitation (see Figs. 8a-b). The area of stratiform precipitation substantially increases in the
299 right-of-shear quadrants of the CTL TC while those quadrants of the S1 TC are almost devoid of
300 stratiform precipitation, which can be inferred from the comparison between Figs. 7a and 7b and
301 clearly seen from one example in Fig. 8.

302 A large patch of low- θ_e air (<358 K) at the lowest model level appears in the upshear-left
303 quadrant near 1800 UTC 2 October and is superimposed by the downward motion (<-0.2 m s⁻¹)
304 at 1-km height at the leading edge of the spiral rainband (Figs. 7c-d). This finding suggests that
305 the low- θ_e air originates from above the boundary layer and is transported downward by
306 convective downdrafts. This low-level ventilation pathway is comparable with the one proposed
307 by Riemer et al. (2010), although they discussed this process in a mature hurricane with a well-
308 defined eyewall. These low- θ_e parcels are then advected downwind and their θ_e gradually
309 recover to higher values during their propagation toward the downshear-right quadrant (i.e.,
310 ~1800-2100 UTC 2 October), indicative of a boundary layer recovery process (Powell 1990;
311 Molinari et al. 2013; Zhang et al. 2013; Nguyen et al. 2019). Multiple low-level ventilation and
312 subsequent boundary layer recovery events can be found in both experiments over the 12-h
313 period. In CTL, the θ_e averaged within the lowest 500 m is generally 2-K warmer than that in S1

314 (cf. Figs. 7c and 7d). Given the inward rebuilding events in CTL are generally stronger than
315 those in S1, a key question arises as whether the stronger newly-developed deep convection in
316 CTL is attributed to the more effective boundary layer recovery for the warmer SST. In the next
317 section, we will address this issue by performing trajectory analyses and along-trajectory vertical
318 momentum budgets.

319 **5. Boundary layer recovery**

320 *a. Trajectory analyses*

321 To examine the role of boundary layer recovery in the inward rebuilding process, a forward
322 Lagrangian trajectory analysis of the downdraft-related low- θ_e air parcels in the lower boundary
323 layer, beneath the leading edge of the CPS, is carried out. The 4-h trajectory analysis starts from
324 1700 UTC and 1740 UTC 2 October for the CTL and S1 TCs, respectively, when the midlevel
325 vortex of both TCs is located upshear (Fig. 1b), and the pattern and intensity of the CPS (Figs. 9a
326 and 9d) as well as the low- θ_e values beneath the rainband are comparable (Figs. 9b-c and 9e-f).
327 Over the 4-h period, precipitation symmetrization is sustained in CTL while it is hindered after
328 1830 UTC 2 October in S1 (Figs. 7a-b). A total of 320 parcels are tracked from the low- θ_e
329 region, with 64 parcels at 3rd, 5th, 7th, 9th, and 11th lowest model levels, respectively. The mean
330 height of all of these 5 model levels is below 450 m. The initial locations of the 64 parcels at
331 each model level are the same (see black dots in Figs. 9a and 9d), and the horizontal spacing
332 between each parcel at the same model level is 4 km. Figures 9b-c and 9e-f show the initial
333 trajectory points colored by the maximum height of the subsequent 4-h forward trajectories. The
334 parcels with their maximum height below 1.5 km are referred to as “boundary layer parcels”
335 (PBL). The others with their maximum height within 1.5-4 km, 4-8 km, and >8 km are grouped
336 into shallow, midlevel, and deep convection categories, respectively, which is analogous to the

337 partitioning of convection in section 2. A comparison of the parcel trajectories starting from the
338 3rd (Figs. 9b-c) and 7th (Figs. 9e-f) lowest model levels between CTL and S1 indicates that the
339 parcels in CTL are more likely to develop into deep convection, while most of the parcels in S1
340 fail to escape from the boundary layer (<1.5 km). Similar results are also found for the
341 trajectories starting from other model levels in the lower boundary layer (not shown). Statistics
342 based on the maximum height of these 4-h trajectories confirm this statement (Fig. 10). More
343 than 80% of the tracked parcels in CTL develop into convection while the ratio decreases ~40%
344 in S1. Moreover, ~35% of these parcels in CTL develop into deep convection while the ratio
345 decreases to <3% in S1. These results are consistent with the difference in the strength of inward
346 rebuilding between the event 4 in CTL and event 3 in S1 (Fig. 6).

347 To quantitatively examine the differences in the trajectories between the two experiments,
348 the top 20% of the tracked parcels based on their maximum height of the 4-h trajectory are
349 selected for a comparison. Figure 11 shows the evolution of height and vertical velocity along
350 the trajectories. Over the first 2 hours of the trajectories ($t = 0-2$ h), these parcels in both CTL
351 and S1 generally stay below 1.5 km height, and their vertical velocity is generally $<1 \text{ m s}^{-1}$. The
352 parcel height evolution in CTL and S1 diverges afterwards (Fig. 11a), as the upward motion of
353 these parcels in CTL accelerates more rapidly than that in S1 (Fig. 11b). Considering these facts,
354 the boundary layer recovery of these parcels over $t = 0-2$ h is examined in Fig. 12. In CTL, the
355 mean θ_e increase over $t = 0-2$ h for these parcels is ~5 K (Fig. 12a). In contrast, the mean θ_e
356 increase in S1 is 1.5 K over the same period, which is 3.6 K lower than that in CTL. Figure 12b
357 further shows that at $t = 0$ h the mean θ_e of these parcels in CTL is 2.1 K cooler than that in S1,
358 while at $t = 2$ h the mean θ_e of these parcels in CTL is 1.5 K warmer. Additionally, the mean
359 parcel height in both experiments is <600 m over $t = 0-2$ h, and mean parcel height in CTL is 190

360 m lower than that in S1 (Fig. 12a). Given that the period of trajectory analyses is before sunrise
 361 at local time (0100-0500 LST for CTL), there is no incoming shortwave radiation; in right-of-
 362 shear quadrants, weak radiative heating is only found in the boundary layer of the downshear-left
 363 quadrant and is one order smaller in magnitude than the diabatic heating due to upward enthalpy
 364 fluxes (not shown). Thus, the upward enthalpy fluxes from the ocean surface is the dominant
 365 energy source in the lower boundary layer; the more efficient boundary layer recovery in CTL is
 366 attributed to the warmer SST as well as the ability of these parcels to stay at a lower height
 367 where the upward enthalpy fluxes are typically larger (Zhang and Drennan 2012).

368 ***b. Along-trajectory vertical momentum budgets***

369 To investigate the mechanisms responsible for the convective initiation and the subsequent
 370 convective development during precipitation symmetrization, a vertical momentum budget along
 371 the trajectories of the top 20% of the tracked parcels is performed for both experiments
 372 (Jeevanjee and Romps 2015):

$$373 \quad \frac{dw}{dt} = a_i + a_b, \quad (1)$$

374 in which w is the vertical velocity and the vertical acceleration ($\frac{dw}{dt}$) is decomposed into dynamic
 375 (a_i) and buoyancy (a_b) accelerations. The buoyancy acceleration (or “effective buoyancy”) is
 376 defined as the Lagrangian acceleration that would result if the wind were instantaneously zeroed
 377 out. Similarly, the dynamic acceleration is defined as the Lagrangian vertical acceleration
 378 resulting from an instantaneous zeroing out of any horizontal density anomalies. The relative
 379 roles of these two acceleration terms could be quantified by solving the Poisson equation:

$$380 \quad -\nabla^2(\bar{\rho}a_b) = g\nabla_h^2\bar{\rho}, \quad (2)$$

$$381 \quad -\nabla^2(\bar{\rho}a_i) = -\partial_z\nabla \cdot [\bar{\rho}(\mathbf{u} \cdot \nabla)\mathbf{u}], \quad (3)$$

382 where $\bar{\rho}$ is horizontal average of air density in the budget domain, ρ is the air density, g is the
 383 gravitational acceleration, and \mathbf{u} is the three-dimensional wind vector, ∇^2 is the three-
 384 dimensional Laplacian operator, and ∇_h^2 is the horizontal Laplacian operator. Dirichlet boundary
 385 conditions of $a_i = 0$ and $a_b = 0$ are specified on the top and bottom boundaries following
 386 Jeevanjee and Romps (2015). The main advantage of this form of vertical momentum budget
 387 over other forms (e.g., Zhang et al. 2000; Braun 2002; Eastin et al. 2005) is that it refrains from
 388 the ambiguity in the arbitrary definition of the reference state $\bar{\rho}$ when calculating the
 389 Archimedean buoyancy (Davies-Jones 2003; Doswell and Markowski 2004). Note that a_b
 390 includes both Archimedean buoyancy and the environment response to vertical acceleration
 391 driven by Archimedean buoyancy. To improve the accuracy of the interpolated vertical
 392 acceleration along the trajectories, the vertical momentum budget is performed from 50 m to 18
 393 km height at a 50-m interval.

394 Figures 13a and 13d show that $\frac{dw}{dt} (=a_i + a_b)$ averaged below 1.5 km height and over $t = 0-$
 395 2 h is marginal in the right-of-shear semicircle. This finding is consistent with the fact that the
 396 top 20% of the tracked parcels stratified by their maximum height of the 4-h trajectory in both
 397 experiments stay in the boundary layer before arriving at the downshear convergence zone. The
 398 a_b within $r = 40$ km is positive in the right-of-shear semicircle below 1.5 km height (Figs. 13c
 399 and 13f), which is largely counteracted by a_i (Figs. 13b and 13e). The mean $\frac{dw}{dt}$ along the
 400 trajectory over $t = 0-2$ h is positive in both experiments (Fig. 14a). Of note, the mean w of the
 401 tracked parcels over the initial half hour is negative in both experiments (Fig. 11b), and negative
 402 $\frac{dw}{dt}$ is not required to retain these parcels in the boundary layer. The larger upward acceleration in
 403 S1 over $t = 0-2$ h is mainly attributed to the much larger a_b in S1 (Fig. 14a), which is further
 404 related to the smaller mean orbital radius (≈ 30 km) in S1 (Fig. 13) such that parcels can tap into

405 the warm reservoir near the TC center (see Fig. 5e-f). In contrast, the mean orbital radius in CTL
406 is 50 km, which is generally outside the region of relatively large a_b ($>0.2 \text{ m s}^{-2}$).

407 The smaller mean $\frac{dw}{dt}$ over $t=0-2 \text{ h}$ in CTL (Fig. 14a) accounts for the lower mean parcel
408 height in CTL than in S1 (Fig. 12a). These parcels subsequently arrive at the inward flank of the
409 CPS, indicated by the spiral band of upward motion at 1.5 km height (Fig. 15), or downshear
410 convergence zone, where both the dynamic and buoyancy forcing play an important role in
411 lifting the parcels out of the boundary layer (i.e., convective initiation). The upward dynamic
412 forcing is likely attributed to the low-level convergence in the downshear convergence zone, and
413 it is difficult to further decompose the dynamical forcing to quantify the relative contribution of
414 the low-level convergence and other mechanisms. The role of dynamic forcing in the convective
415 initiation in the incipient eyewall is consistent with the findings in previous modeling studies of
416 TCs (Zhang et al. 2000; Braun 2002; Gu et al. 2019). *One new finding in this study is that the*
417 *buoyancy forcing also plays a role in the convective initiation at the inward flank of the CPS*
418 (Figs. 15c and 15f). Figures 15 and 11 also indicate a striking difference between the two
419 experiments: in CTL a large portion of these parcels have already developed or are going to
420 develop into deep convection in the downwind part of the azimuthally-propagating CPS, as seen
421 in Figs. 4-6, while in S1 the parcels reaching the downwind part of the CPS mostly develop into
422 shallow and midlevel convection.

423 Figure 14b shows the vertical acceleration terms averaged over $t = 2-3 \text{ h}$ for the top 20% of
424 the tracked parcels. Both the a_b and $\frac{dw}{dt}$ are significantly larger than those over $t=0-2 \text{ h}$ (Fig. 14a).
425 Clearly, the acceleration of the upward motion above the boundary layer is mainly attributed to
426 the a_b in both experiments. Parcels in CTL exhibit larger mean a_b over $t = 2-3 \text{ h}$ than those in
427 S1, which is mainly attributed to the stronger a_b over $t = 2.5-3 \text{ h}$ in CTL (see Fig. 16). In S1, a_i

428 plays a secondary role in accelerating the upward motion; whereas in CTL, the mean a_i for these
429 parcels is negative (Fig. 14b). Figure 16 further shows that in both experiments dynamic forcing
430 accelerates the upward motion of parcels over $t = 2-2.5$ h, when these parcels still reside at low
431 levels; as convection matures over $t = 2.5-3$ h, these parcels experience substantial dynamic
432 deceleration. The dynamical deceleration in CTL is more notable over $t = 2.5-3$ h, leading to a
433 net negative value of a_i over $t = 2-3$ h in CTL (Fig. 14b). The dynamical deceleration comes
434 from the effect of a downward-pointing perturbation pressure gradient force (cf. Braun 2002). In
435 short, the stronger acceleration of the upward motion during the convective development in CTL
436 is attributed to the stronger a_b . Given the a_b during convective development is closely related to
437 the θ_e values of the parcels at convective initiation, the above findings confirm that the boundary
438 layer recovery of the downdraft-cooled parcels is a key mechanism in maintaining the convective
439 activity during precipitation symmetrization.

440 **6. Discussion**

441 *a. Observational support and additional discussions on precipitation symmetrization*

442 As mentioned in section 4, the successive inward rebuilding of the CPS during precipitation
443 symmetrization under moderate VWS is reminiscent of the observed “inward progression” of the
444 cloud-to-ground lightning clusters in the RI TCs under moderate VWS (e.g., Molinari et al.
445 2004; Molinari and Vollaro 2010; Stevenson et al. 2014; Zawislak et al. 2016). Note that cloud-
446 to-ground lightning can be treated as an indicator of strong/deep convection. These observational
447 case studies clearly show that during precipitation symmetrization the lightning cluster drifted
448 cyclonically from downshear-left at *large* radii to upshear-left at *smaller* radii and mostly inside
449 the RMW. The relationship between boundary layer recovery and convective development in the

450 sheared TCs was also alluded to in observational studies of Tropical Storm Edouard (2002)
451 (Molinari et al. 2013), Hurricane Cristobal and Bertha (2014) (Nguyen et al. 2017), and early-
452 stage TCs from 1997 to 2017 (see fig. 16 in Nguyen et al. 2019). These observational facts imply
453 that the identified “inward rebuilding” pathway is not limited to one single sheared TC, and the
454 related the dynamical (e.g., downshear convergence zone and the associated low-level
455 convergence) and thermodynamic processes (e.g., boundary layer recovery) are intrinsic to
456 sheared early-stage TCs.

457 Previous observational studies (e.g., Molinari et al. 2013; Nguyen et al. 2017) generally
458 recognized that the high- θ_e parcels in the downshear-right quadrant contribute to the convective
459 development in the left-of-shear quadrants of sheared TCs. However, to our knowledge, no direct
460 evidence has been presented to prove that the downshear-right high- θ_e parcels that contribute to
461 the subsequent left-of-shear convective development are an outcome of the boundary layer
462 recovery of downdraft-cooled parcels beneath the CPS at earlier times. Thus, one unique
463 contribution of this study is that the identified “inward rebuilding” pathway directly relates the
464 boundary layer recovery of downdraft-cooled parcels to the development of deep convection in
465 the left-of-shear quadrants. Additionally, observational and modeling studies of TCs in shear
466 frequently pointed out the deep convection in the upshear quadrant and inside the RMW as a key
467 factor in differentiating the RI and non-RI TCs (e.g., Rogers et al. 2016; Hazelton et al. 2017;
468 Wadler et al. 2018a; Leighton et al. 2018), while mechanisms responsible for the radius and
469 quadrant preference of deep convection for RI TCs remain elusive. The “inward rebuilding”
470 pathway provides a reasonable explanation to this phenomenon. This pathway is considered
471 applicable to the sheared TCs at tropical storm or minimal hurricane stage, when the eyewall has

472 not yet typically formed, but when RI occurs more frequently (Kaplan et al. 2010; Chen et al.
473 2015).

474 Over warm SST, the CTL TC also has a much larger area of stratiform precipitation in the
475 right-of-shear quadrants than the S1 TC after 1800 UTC 2 October (Figs. 7a-b, 8, and 17a-b).
476 Figure 17 shows azimuthal-height plots of radar reflectivity, θ_e , relative humidity, and vertical
477 velocity averaged within $r = 20\text{-}60$ km and over the period of 1800-1850 UTC 2 October for the
478 CTL and S1 TCs. Given stratiform precipitation is preferred in an environment with high
479 saturation fraction (López and Raymond 2005), the prevailing stratiform precipitation in the
480 right-of-shear quadrants of the CTL TC suggest the inner-core environment therein is very moist,
481 as seen from the nearly saturated 5-9 km layer above the freezing level (cf. Figs. 17c-d). In
482 contrast, the RH of the 5-9 km layer in the right-of-shear quadrants of the S1 TC is $<85\%$. An
483 idealized simulation study (Rios-Berrios et al. 2018) also found that the right-of-shear quadrants
484 of the TC inner core become very moist before RI onset. The humidification of the layer above
485 the freezing level in the right-of-shear quadrants is most likely attributed to the horizontal
486 advection of water vapor and the evaporation/sublimation of condensates coming from the
487 upwind quadrants (Rappin and Nolan 2012; Alvey et al. 2020). All of these processes are closely
488 related to the convection that transports the boundary layer moisture upward into the mid-to-
489 upper troposphere. The left-of-shear convective activity within the inner core is generally more
490 vigorous in CTL than in S1 over the 12-h period preceding the RI onset of the CTL TC (Figs. 7a-
491 b), which helps account for the more moist midlevels in the right-of-shear quadrants of the CTL
492 TC. In the numerical simulation study of Typhoon Vicente (2012), the amount of deep
493 convection in upshear quadrants steadily increases 5 hours before RI onset (Chen et al. 2018b)
494 and a nearly-saturated inner core forms at RI onset (Chen et al. 2019), which lends support to the

495 hypothesis. A detailed diagnostic analysis of the moistening processes in a shear-relative
496 framework is beyond the scope of this study and will be left for future work.

497 ***b. Comparison with a mesoscale convective system with trailing stratiform***

498 The analyses in section 5 demonstrate that the precipitation symmetrization of the sheared
499 TCs is essentially a three-dimensional rather than an axisymmetric process (also see Fig. 18).
500 Particularly, the boundary layer recovery of downdraft-cooled parcels and the subsequent inward
501 rebuilding of deep convection in the sheared TCs cannot be described in the simulations using an
502 axisymmetric framework. Before the formation of a complete eyewall, the CPS propagates
503 cyclonically and radially inward during precipitation symmetrization. The CPS in a sheared
504 early-stage TC is analogous to a midlatitude mesoscale convective system with trailing stratiform
505 (hereafter MCS-TS, Parker and Johnson 2000) in both morphology and organization, with
506 ascending flow in the front (radially inward in a TC) of the moving MCS-TS and descending
507 inflow from the rear (radially outward in a TC) and below the freezing level (Fig. 18d).

508 However, the CPS in a sheared TC differs from MCS-TS due to its imposed swirling
509 circulation of the TC. In the mature stage of MCS-TS, convective updrafts are sustained by the
510 high- θ_e inflow in the front, and the cold pool (i.e., low- θ_e) region remains in the rear flank of the
511 convective system that induces low-level convergence for the convective updrafts. In a sheared
512 TC, however, the downdraft-induced low- θ_e parcels are “recycled” in the TC circulation,
513 gradually recovered by positive enthalpy fluxes, slowly ascend in the boundary layer (e.g., see
514 the newly-formed spiral rainband along the trajectory in Fig. 18a) during their advection toward
515 the downshear convergence zone, and ultimately become a part of the ascending branch radially
516 inward of the downwind part of the CPS if their entropy has been sufficiently recovered. This
517 scenario is seen in both TCs (Figs. 18b-e), while the newly-developed convection in the inward

518 rebuilding events is weaker in the S1 TC. This conceptual model in Fig. 18 highlights the critical
519 role of warm SST and boundary layer recovery in replenishing these low- θ_e parcels and favoring
520 the symmetrization of the CPS in the sheared TCs prior to the formation of a closed eyewall.

521 An important implication of this study is that the low-level ventilation does not necessarily
522 weaken the early-stage TCs over warm SSTs; instead, the competition between the low-level
523 ventilation and boundary layer recovery matters to the subsequent convective activity and
524 structural/intensity change of the early-stage TCs in VWS.

525 **7. Concluding remarks**

526 Precipitation symmetrization or eyewall formation preceding the rapid intensification (RI)
527 of tropical cyclones (TCs) under moderate vertical wind shear (VWS) has been documented in
528 recent studies (e.g., Zagrodnik and Jiang 2014; Tao and Jiang 2015; Alvey et al. 2015; Tao et al.
529 2017; Chen et al. 2017; Fischer et al. 2018). Understanding thermodynamic/dynamical
530 mechanisms controlling the precipitation symmetrization is the central question addressed in this
531 study. By analyzing two representative numerical simulations of Typhoon Mujigae (2015),
532 initialized with warm (i.e., CTL) and relatively cool (i.e., S1) SSTs, respectively, key results are
533 summarized as follows:

534 1) A downshear convergence zone forms due to the differential advection by the VWS. The
535 convective precipitation shield (CPS) is initially embedded in this convergence zone and
536 subsequently propagates into the upshear side before RI onset. Downdraft-cooled parcels beneath
537 the CPS are advected downwind by the swirling winds and their entropy is gradually recovered
538 by positive enthalpy fluxes (i.e., boundary layer recovery).

539 2) The boundary layer recovery is key to the convective development and precipitation
540 symmetrization before RI onset. Trajectory analyses of the downdraft-cooled parcels and the

541 along-trajectory vertical momentum budget demonstrate that the boundary layer recovery is
542 more efficient in CTL due to the warmer SST, and the resulting stronger buoyancy acceleration
543 are responsible for the development of much more deep convection in CTL than in S1,
544 particularly in the upshear quadrants. Additionally, downdraft-cooled parcels are lifted out of the
545 boundary layer by both dynamical and buoyancy acceleration in the convergence zone (i.e.,
546 convective initiation).

547 3) The precipitation symmetrization before RI onset in both experiments is maintained by
548 the continuous development of deep convection radially inward of the azimuthally propagating
549 CPS (i.e., inward rebuilding event), as deep convection matures in the downwind part of the
550 CPS. In CTL, precipitation symmetrization is sustained by stronger newly-developed deep
551 convection in successive inward rebuilding events, and the associated stronger microphysics
552 diabatic heating inside/near the radius of the maximum wind (RMW) aids in the earlier RMW
553 contraction of the CTL TC (see discussions in Chen et al. 2018a). In contrast, precipitation
554 symmetrization is delayed in S1 due to the weaker newly-developed convection radially inward
555 of the CPS, particularly in the upshear-left quadrant, and the RMW contraction is also delayed.

556 These above processes form a positive feedback between boundary layer recovery, *inward*
557 *rebuilding of the CPS*, precipitation symmetrization, and RMW contraction under the warmer
558 SST, and highlight the key role of the boundary layer recovery of the downdraft-cooled parcels
559 in alleviating the low-level ventilation and organizing the CPS during precipitation
560 symmetrization. Additionally, these results provide an explanation for the frequently observed
561 deep convection in the upshear quadrant and inside the RMW of the sheared TCs before RI
562 onset.

563 **Acknowledgments:** This research had been supported by the National Key R&D Program of
564 China under Grant 2017YFC1501601, the Natural Science Foundation of China Grants

565 41875067 and 41605033. We want to acknowledge Drs. Jon Zawislak, Andy Hazelton, and Paul
566 Reasor for their helpful suggestions to the early version of the paper. Discussions with Prof. Juan
567 Fang and Dr. Michael Fischer also provided valuable insight into the analysis. The first author
568 Xiaomin Chen is supported by the NRC Research Associateship Programs. Jun A. Zhang is
569 supported by NOAA grant NA14NWS4680030 and NSF grant AGS-1822128.

570

571 **References**

- 572 Alvey III, G. R., J. Zawislak, and E. Zipser, 2015: Precipitation properties observed during
 573 tropical cyclone intensity change. *Mon. Wea. Rev.*, **143**, 4476-4492.
- 574 Alvey, G. R., III, E. Zipser, and J. Zawislak, 2020: How does Hurricane Edouard (2014) evolve
 575 toward symmetry before rapid intensification? A high-resolution ensemble study. *J. Atmos.*
 576 *Sci.*, **77**, 1329-1351.
- 577 Bhatia, K. T., and D. S. Nolan, 2013: Relating the skill of tropical cyclone intensity forecasts to
 578 the synoptic environment. *Wea. Forecasting*, **28**, 961-980.
- 579 Bender, M. A., 1997: The effect of relative flow on the asymmetric structure in the interior of
 580 hurricanes. *J. Atmos. Sci.*, **54**, 703-724.
- 581 Bracken, W. E., and L. F. Bosart, 2000: The role of synoptic-scale flow during tropical
 582 cyclogenesis over the North Atlantic Ocean. *Mon. Wea. Rev.*, **128**, 353-376.
- 583 Braun, S. A., 2002: A cloud-resolving simulation of hurricane bob (1991): Storm structure and
 584 eyewall buoyancy. *Mon. Wea. Rev.*, **130**, 1573-1592.
- 585 Chen, X., Y. Wang, and K. Zhao, 2015: Synoptic flow patterns and large-scale characteristics
 586 associated with rapidly intensifying tropical cyclones in the South China Sea. *Mon. Wea.*
 587 *Rev.*, **143**, 64-87.
- 588 Chen, X., M. Xue, and J. Fang, 2018a: Rapid intensification of Typhoon Mujigae (2015) under
 589 different sea surface temperatures: Structural changes leading to rapid intensification. *J.*
 590 *Atmos. Sci.*, **75**, 4313-4335.
- 591 Chen, X., J. A. Zhang, and F. D. Marks, 2019: A thermodynamic pathway leading to rapid
 592 intensification of tropical cyclones in shear. *Geophys. Res. Lett.*, **46**, 9241-9251.
- 593 Chen, X., Y. Wang, K. Zhao, and D. Wu, 2017: A numerical study on rapid intensification of
 594 Typhoon Vicente (2012) in the South China Sea. Part I: Verification of simulation, storm-
 595 scale evolution, and environmental contribution. *Mon. Wea. Rev.*, **145**, 877-898.
- 596 Chen, X., Y. Wang, J. Fang, and M. Xue, 2018b: A numerical study on rapid intensification of
 597 Typhoon Vicente (2012) in the South China Sea. Part II: Roles of inner-core processes. *J.*
 598 *Atmos. Sci.*, **75**, 235-255.
- 599 Corbosiero, K. L., and J. Molinari, 2002: The effects of vertical wind shear on the distribution of
 600 convection in tropical cyclones. *Mon. Wea. Rev.*, **130**, 2110-2123.
- 601 Davies-Jones, R., 2003: An expression for effective buoyancy in surroundings with horizontal
 602 density gradients. *J. Atmos. Sci.*, **60**, 2922-2925.
- 603 DeMaria, M., C. R. Sampson, J. A. Knaff, and K. D. Musgrave, 2014: Is tropical cyclone
 604 intensity guidance improving? *Bull. Am. Meteorol. Soc.*, **95**, 387-398.
- 605 Doswell, C. A., and P. Markowski, 2004: Is buoyancy a relative quantity? *Mon. Wea. Rev.*, **132**,
 606 853-863.
- 607 Eastin, M. D., W. M. Gray, and P. G. Black, 2005: Buoyancy of convective vertical motions in
 608 the inner core of intense hurricanes. Part II: Case studies. *Mon. Wea. Rev.*, **133**, 209-227.
- 609 Fischer, M. S., B. H. Tang, K. L. Corbosiero, and C. M. Rozoff, 2018: Normalized convective
 610 characteristics of tropical cyclone rapid intensification events in the north atlantic and
 611 eastern north pacific. *Mon. Wea. Rev.*, **146**, 1133-1155.
- 612 Fritz, C., Z. Wang, W. Nesbitt Stephen, and J. Dunkerton Timothy, 2016: Vertical structure and
 613 contribution of different types of precipitation during Atlantic tropical cyclone formation as
 614 revealed by TRMM PR. *Geophys. Res. Lett.*, **43**, 894-901.
- 615 Gu, J.-F., Z.-M. Tan, and X. Qiu, 2015: Effects of vertical wind shear on inner-core
 616 thermodynamics of an idealized simulated tropical cyclone. *J. Atmos. Sci.*, **72**, 511-530.

- 617 Gu, J.-F., Z.-M. Tan, and X. Qiu, 2019: Intensification variability of tropical cyclones in
618 directional shear flows: Vortex tilt–convection coupling. *J. Atmos. Sci.*, **76**, 1827-1844.
- 619 Jeevanjee, N., and D. M. Romps, 2015: Effective buoyancy, inertial pressure, and the mechanical
620 generation of boundary layer mass flux by cold pools. *J. Atmos. Sci.*, **72**, 3199-3213.
- 621 Jones, S. C., 1995: The evolution of vortices in vertical shear. I: Initially barotropic vortices.
622 *Quart. J. Roy. Meteor. Soc.*, **121**, 821-851.
- 623 —, 2004: On the ability of dry tropical-cyclone-like vortices to withstand vertical shear. *J.*
624 *Atmos. Sci.*, **61**, 114-119.
- 625 Judt, F., and S. S. Chen, 2016: Predictability and dynamics of tropical cyclone rapid
626 intensification deduced from high-resolution stochastic ensembles. *Mon. Wea. Rev.*, **144**,
627 4395-4420.
- 628 Kaplan, J., M. DeMaria, and J. A. Knaff, 2010: A revised tropical cyclone rapid intensification
629 index for the Atlantic and Eastern North Pacific basins. *Wea. Forecasting*, **25**, 220-241.
- 630 Leighton, H., S. Gopalakrishnan, J. A. Zhang, R. F. Rogers, Z. Zhang, and V. Tallapragada, 2018:
631 Azimuthal distribution of deep convection, environmental factors, and tropical cyclone
632 rapid intensification: A perspective from HWRF ensemble forecasts of Hurricane Edouard
633 (2014). *J. Atmos. Sci.*, **75**, 275-295.
- 634 López Carrillo, C., and D. J. Raymond, 2005: Moisture tendency equations in a tropical
635 atmosphere. *J. Atmos. Sci.*, **62**, 1601-1613.
- 636 Miyamoto, Y., and D. S. Nolan, 2018: Structural changes preceding rapid intensification in
637 tropical cyclones as shown in a large ensemble of idealized simulations. *J. Atmos. Sci.*, **75**,
638 555-569.
- 639 Molinari, J., and D. Vollaro, 2010: Rapid intensification of a sheared tropical storm. *Mon. Wea.*
640 *Rev.*, **138**, 3869-3885.
- 641 Molinari, J., D. Vollaro, and K. L. Corbosiero, 2004: Tropical cyclone formation in a sheared
642 environment: A case study. *J. Atmos. Sci.*, **61**, 2493-2509.
- 643 Molinari, J., J. Frank, and D. Vollaro, 2013: Convective bursts, downdraft cooling, and boundary
644 layer recovery in a sheared tropical storm. *Mon. Wea. Rev.*, **141**, 1048-1060.
- 645 Molinari, J., P. Dodge, D. Vollaro, K. L. Corbosiero, and F. Marks, 2006: Mesoscale aspects of
646 the downshear reformation of a tropical cyclone. *J. Atmos. Sci.*, **63**, 341-354.
- 647 Nguyen, L. T., and J. Molinari, 2015: Simulation of the downshear reformation of a tropical
648 cyclone. *J. Atmos. Sci.*, **72**, 4529-4551.
- 649 Nguyen, L. T., J. Molinari, and D. Thomas, 2014: Evaluation of tropical cyclone center
650 identification methods in numerical models. *Mon. Wea. Rev.*, **142**, 4326-4339.
- 651 Nguyen, L. T., R. F. Rogers, and P. D. Reasor, 2017: Thermodynamic and kinematic influences
652 on precipitation symmetry in sheared tropical cyclones: Bertha and Cristobal (2014). *Mon.*
653 *Wea. Rev.*, **145**, 4423-4446.
- 654 Nguyen, L. T., R. Rogers, J. Zawislak, and J. A. Zhang, 2019: Assessing the influence of
655 convective downdrafts and surface enthalpy fluxes on tropical cyclone intensity change in
656 moderate vertical wind shear. *Mon. Wea. Rev.*
- 657 Onderlinde, M. J., and D. S. Nolan, 2016: Tropical cyclone–relative environmental helicity and
658 the pathways to intensification in shear. *J. Atmos. Sci.*, **73**, 869-890.
- 659 Parker, M. D., and R. H. Johnson, 2000: Organizational modes of midlatitude mesoscale
660 convective systems. *Mon. Wea. Rev.*, **128**, 3413-3436.
- 661 Pendergrass, A. G., and H. E. Willoughby, 2009: Diabatically induced secondary flows in
662 tropical cyclones. Part I: Quasi-steady forcing. *Mon. Wea. Rev.*, **137**, 805-821.

- 663 Powell, M. D., 1990: Boundary layer structure and dynamics in outer hurricane rainbands. Part
 664 II: Downdraft modification and mixed layer recovery. *Mon. Wea. Rev.*, **118**, 918-938.
- 665 Rappin, E. D., and D. S. Nolan, 2012: The effect of vertical shear orientation on tropical
 666 cyclogenesis. *Quart. J. Roy. Meteor. Soc.*, **138**, 1035-1054.
- 667 Reasor, P. D., R. Rogers, and S. Lorsolo, 2013: Environmental flow impacts on tropical cyclone
 668 structure diagnosed from airborne Doppler radar composites. *Mon. Wea. Rev.*, **141**, 2949-
 669 2969.
- 670 Riemer, M., M. T. Montgomery, and M. E. Nicholls, 2010: A new paradigm for intensity
 671 modification of tropical cyclones: Thermodynamic impact of vertical wind shear on the
 672 inflow layer. *Atmos. Chem. Phys.*, **10**, 3163-3188.
- 673 —, 2013: Further examination of the thermodynamic modification of the inflow layer of tropical
 674 cyclones by vertical wind shear. *Atmos. Chem. Phys.*, **13**, 327-346.
- 675 Rios-Berrios, R., C. A. Davis, and R. D. Torn, 2018: A hypothesis for the intensification of
 676 tropical cyclones under moderate vertical wind shear. *J. Atmos. Sci.*, **75**, 4149-4173.
- 677 Rogers, R., 2010: Convective-scale structure and evolution during a high-resolution simulation
 678 of tropical cyclone rapid intensification. *J. Atmos. Sci.*, **67**, 44-70.
- 679 Rogers, R. F., J. A. Zhang, J. Zawislak, H. Jiang, G. R. Alvey, E. J. Zipser, and S. N. Stevenson,
 680 2016: Observations of the structure and evolution of Hurricane Edouard (2014) during
 681 intensity change. Part II: Kinematic structure and the distribution of deep convection. *Mon.*
 682 *Wea. Rev.*, **144**, 3355-3376.
- 683 Rogers, R. F., P. D. Reasor, J. A. Zawislak, and L. T. Nguyen, 2020: Precipitation processes and
 684 vortex alignment during the intensification of a weak tropical cyclone in moderate vertical
 685 shear. *Mon. Wea. Rev.*, **148**, 1899-1929.
- 686 Ryglicki, D. R., J. D. Doyle, Y. Jin, D. Hodyss, and J. H. Cossuth, 2018: The unexpected rapid
 687 intensification of tropical cyclones in moderate vertical wind shear. Part II: Vortex tilt. *Mon.*
 688 *Wea. Rev.*, **146**, 3801-3825.
- 689 Schechter, D. A., 2020: Distinct intensification pathways for a shallow-water vortex subjected to
 690 asymmetric “diabatic” forcing. *Dyn. Atmos. Oceans*, 101156.
- 691 Schubert, W. H., and J. J. Hack, 1982: Inertial stability and tropical cyclone development. *J.*
 692 *Atmos. Sci.*, **39**, 1687-1697.
- 693 Shimada, U., and T. Horinouchi, 2018: Reintensification and eyewall formation in strong shear:
 694 A case study of Typhoon Noul (2015). *Mon. Wea. Rev.*, **146**, 2799-2817.
- 695 Stevenson, S. N., K. L. Corbosiero, and J. Molinari, 2014: The convective evolution and rapid
 696 intensification of Hurricane Earl (2010). *Mon. Wea. Rev.*, **142**, 4364-4380.
- 697 Tang, B., and K. Emanuel, 2010: Midlevel ventilation’s constraint on tropical cyclone intensity.
 698 *J. Atmos. Sci.*, **67**, 1817-1830.
- 699 —, 2012: Sensitivity of tropical cyclone intensity to ventilation in an axisymmetric model. *J.*
 700 *Atmos. Sci.*, **69**, 2394-2413.
- 701 Tang, X., Z.-M. Tan, J. Fang, E. B. Munsell, and F. Zhang, 2019: Impact of the diurnal radiation
 702 contrast on the contraction of radius of maximum wind during intensification of Hurricane
 703 Edouard (2014). *J. Atmos. Sci.*, **76**, 421-432.
- 704 Tao, C., and H. Jiang, 2015: Distributions of shallow to very deep precipitation–convection in
 705 rapidly intensifying tropical cyclones. *J. Clim.*, **28**, 8791-8824.
- 706 Tao, C., H. Jiang, and J. Zawislak, 2017: The relative importance of stratiform and convective
 707 rainfall in rapidly intensifying tropical cyclones. *Mon. Wea. Rev.*, **145**, 795-809.

708 Tao, D., and F. Zhang, 2014: Effect of environmental shear, sea-surface temperature, and ambient
709 moisture on the formation and predictability of tropical cyclones: An ensemble-mean
710 perspective. *J. Adv. Model. Earth Syst.*, **6**, 384-404.

711 Wadler, J. B., R. F. Rogers, and P. D. Reasor, 2018a: The relationship between spatial variations
712 in the structure of convective bursts and tropical cyclone intensification as determined by
713 airborne Doppler radar. *Mon. Wea. Rev.*, **146**, 761-780.

714 Wadler, J. B., J. A. Zhang, B. Jaimes, and L. K. Shay, 2018b: Downdrafts and the evolution of
715 boundary layer thermodynamics in Hurricane Earl (2010) before and during rapid
716 intensification. *Mon. Wea. Rev.*, **146**, 3545-3565.

717 Wang, Y., and G. J. Holland, 1996: Tropical cyclone motion and evolution in vertical shear. *J.*
718 *Atmos. Sci.*, **53**, 3313-3332.

719 Zagrodnik, J. P., and H. Jiang, 2014: Rainfall, convection, and latent heating distributions in
720 rapidly intensifying tropical cyclones. *J. Atmos. Sci.*, **71**, 2789-2809.

721 Zawislak, J., H. Jiang, G. R. Alvey, E. J. Zipser, R. F. Rogers, J. A. Zhang, and S. N. Stevenson,
722 2016: Observations of the structure and evolution of Hurricane Edouard (2014) during
723 intensity change. Part I: Relationship between the thermodynamic structure and
724 precipitation. *Mon. Wea. Rev.*, **144**, 3333-3354.

725 Zhang, D.-L., Y. Liu, and M. K. Yau, 2000: A multiscale numerical study of hurricane andrew
726 (1992). Part III: Dynamically induced vertical motion. *Mon. Wea. Rev.*, **128**, 3772-3788.

727 Zhang, F., and D. Tao, 2013: Effects of vertical wind shear on the predictability of tropical
728 cyclones. *J. Atmos. Sci.*, **70**, 975-983.

729 Zhang, J. A., and W. M. Drennan, 2012: An observational study of vertical eddy diffusivity in the
730 hurricane boundary layer. *J. Atmos. Sci.*, **69**, 3223-3236.

731 Zhang, J. A., and R. F. Rogers, 2019: Effects of parameterized boundary layer structure on
732 hurricane rapid intensification in shear. *Mon. Wea. Rev.*, **147**, 853-871.

733 Zhang, J. A., R. F. Rogers, P. D. Reasor, E. W. Uhlhorn, and F. D. Marks, 2013: Asymmetric
734 hurricane boundary layer structure from dropsonde composites in relation to the
735 environmental vertical wind shear. *Mon. Wea. Rev.*, **141**, 3968-3984.

736 Zhang, J. A., J. J. Cione, E. A. Kalina, E. W. Uhlhorn, T. Hock, and J. A. Smith, 2017b:
737 Observations of infrared sea surface temperature and air-sea interaction in Hurricane
738 Edouard (2014) using GPS dropsondes. *J. Atmos. Oceanic Technol.*, **34**, 1333-1349.

739 Zipser, E.J., 1969: The role of organized unsaturated convective downdrafts in the structure and
740 rapid decay of an equatorial disturbance. *J. Appl. Meteor.*, **8**, 799-814.

741
742

743 Table 1: Experiment descriptions.

Description	
CTL	Initialized with the SST at 0000 UTC October 2, 2015.
S1	Initialized with the 1990-2013 monthly-mean SST.

744

745

746

747

748 **Figure captions**

749 Fig. 1. Verification of simulated 10-m maximum wind speed (m s^{-1}) in the CTL (red) and S1
750 (black) experiments against the best track data of China Meteorological Administration
751 (gray line with circles). (b) Evolution of the 450-850 hPa vortex tilt magnitude (km) for the
752 CTL and S1 TCs from 1200 UTC 2 October to 1200 UTC 4 October. The three dashed lines
753 mark the downshear-left (DL), upshear-left (UL), and upshear-right (UR) quadrants that the
754 tilt vector points toward. Evolution of (c) local Rossby number R_o and (d) RMW (km) at
755 10-m height for the CTL and S1 TCs. The gray line in (c) denotes $R_o = 12$. The red (black)
756 arrows in each panel denote the RI onset timing of CTL (S1) TC. Adapted from Chen et al.
757 (2018a).

758 Fig. 2. (a)-(c) The 1.5-km radar reflectivity (shading; dBZ), background horizontal convergence
759 (dashed contours with values of -2.0 , -1.0 , $-0.5 \times 10^{-4} \text{ s}^{-1}$), and storm-relative winds (vector,
760 m s^{-1}) at (a) 1600 UTC 2 October, (b) 1800 UTC 2 October, and (c) 2100 UTC 2 October
761 in CTL. (d)-(f) As in (a)-(c), but for S1.

762 Fig. 3. (a)-(b) The location of deep convection within $r = 100$ km relative to the surface TC
763 center (black star) occurred over 1200-1500 UTC 2 October (black plus), 1500-1800 UTC 2
764 October (blue plus), and 1800-2100 UTC 2 October (red plus) in CTL and S1, respectively.
765 (c)-(d) As in (a)-(b), but for the location of CBs. The black arrow in (a)-(d) denotes the 300-
766 850 hPa vertical wind shear. Azimuthal distribution of the number of (e) grid points of deep
767 convection and (f) CBs in CTL (red) and S1 (black) within $r = 60$ km accumulated over
768 1200-2100 UTC 2 October at a 10-min interval. The total number of deep convection and
769 CBs in CTL and S1 are shown as texts. The shear-relative quadrants are labeled in each
770 panel. DR, UR, UL, and DL denote downshear-right, upshear-right, upshear-left and
771 downshear-left quadrant, respectively.

772 Fig. 4. (a)-(f) Evolution of radar reflectivity (shading, dBZ) and storm-relative wind (vector, m s^{-1})
773 at the lowest model level for the CTL TC from 1710 UTC 2 October to 1830 UTC 2
774 October. (g)-(l) As in (a)-(f), but for the S1 TC from 1920 UTC 2 October to 2030 UTC 4
775 October. The solid black circle denote the 50-km reference radius. The dashed black ellipse
776 tracks the propagation of the developing convection inside of the RMW. The reference
777 vector is shown in (a). The gray arrow on the top right corner denotes the heading of 200-
778 850 hPa VWS.

779 Fig. 5. (a)-(b) Plan view of radar reflectivity (shading, dBZ) and storm-relative wind (vector, m s^{-1})
780 at the lowest model level at 1800 UTC 2 October for the CTL and at 2000 UTC 2
781 October for the S1 TC, respectively. (c)-(d) Composite vertical slice of microphysics
782 diabatic heating (shading, K h^{-1}) and absolute vorticity (contoured at 0.5, 1, and $2 \times 10^{-3} \text{ s}^{-1}$)
783 over 1800-1850 UTC 2 October and over 2000-2050 UTC 2 October for the CTL and S1
784 TCs, respectively; (e)-(f) As in (c)-(d), but for θ_e (shading, K) and storm-relative wind
785 (streamline). The position of the vertical slice in (c)-(f) is marked as black dash line in (a)-
786 (b). The white arrow in (a)-(d) marks the location of the newly-formed deep convection.
787 The red streamline in (e)-(f) is related to the newly-developed deep convection inside the
788 RMW.

789 Fig. 6. (a)-(b) Time-radius plot of radar reflectivity (shading, dBZ) averaged azimuthally within
790 the downshear quadrants and below 500 m height from 1200 UTC 2 October to 0000 UTC
791 3 October for the CTL and S1 TCs, respectively. The black dashed lines in each panel

792 denote the visually trackable outward propagation of newly-formed convection within the
793 RMW.

794 Fig. 7. (a)-(b) Time-azimuthal plot of radar reflectivity (shading, dBZ) for the CTL and S1 TCs,
795 respectively. (c)-(d) As in (a)-(b), but for θ_e (shading, K) and vertical velocity (contours
796 with values of $-0.2, 0.2,$ and 0.5 m s^{-1} and negative values are dashed) for the two TCs. The
797 radar reflectivity and θ_e are averaged within $r = 20\text{-}50 \text{ km}$ and below 500-m height. The
798 vertical velocity is averaged within $r = 20\text{-}50 \text{ km}$ at 1-km height. The solid white line
799 denotes the heading direction of $200\text{-}850 \text{ hPa}$ VWS. The dashed white line marks the shear-
800 relative quadrants, as labeled at the bottom of each panel. DR, UR, UL, and DL denote
801 downshear-right, upshear-right, upshear-left and downshear-left quadrant, respectively.

802 Fig. 8. Plan view of (a) radar reflectivity (shading, dBZ) at 3-km height and (b) precipitation
803 mode at 1830 UTC 2 October. The red, yellow, and purple area in (b) denote convective,
804 stratiform, and other type precipitation, respectively. (c)-(d) As in (a)-(b), but for S1 TC.
805 The solid black arrow in (a)-(d) denotes the heading direction of $200\text{-}850 \text{ hPa}$ VWS.

806 Fig. 9. Plan view of (a) radar reflectivity (shading, dBZ) at the 3^{rd} lowest model level, θ_e
807 (shading, K) at the (b) 3^{rd} and (c) 7^{th} lowest model levels at 1700 UTC 2 October for the
808 CTL TC. (d)-(f) As in (a)-(c), but for the S1 TC at 1740 UTC . The location of the initial
809 points of the trajectories are shown as black dots in (a) and (d), and are shown as colored
810 dots based on the maximum height of the subsequent 4-h forward trajectory in (b)-(c) and
811 (e)-(f). Black cross (\times) denotes the boundary layer parcels with the maximum height <1.5
812 km. Pink, red, and violet dots denote the maximum height of these parcels within $1.5\text{-}4 \text{ km}$,
813 $4\text{-}8 \text{ km}$, and $>8 \text{ km}$, respectively. The large black dot at $(0, 0)$ marks the surface TC center.
814 The black circle represents the RMW near the surface. The orange box in (a) and (e)
815 denotes the same area of (b)-(c) and (e)-(f), respectively. The mean height of each model
816 level is shown in the title of each panel.

817 Fig. 10. Bar plot of the ratio of the track parcels that remain in the boundary layer (gray) or
818 develop into the shallow (pink), midlevel (red) and deep (purple) convection in the CTL and
819 S1 experiments.

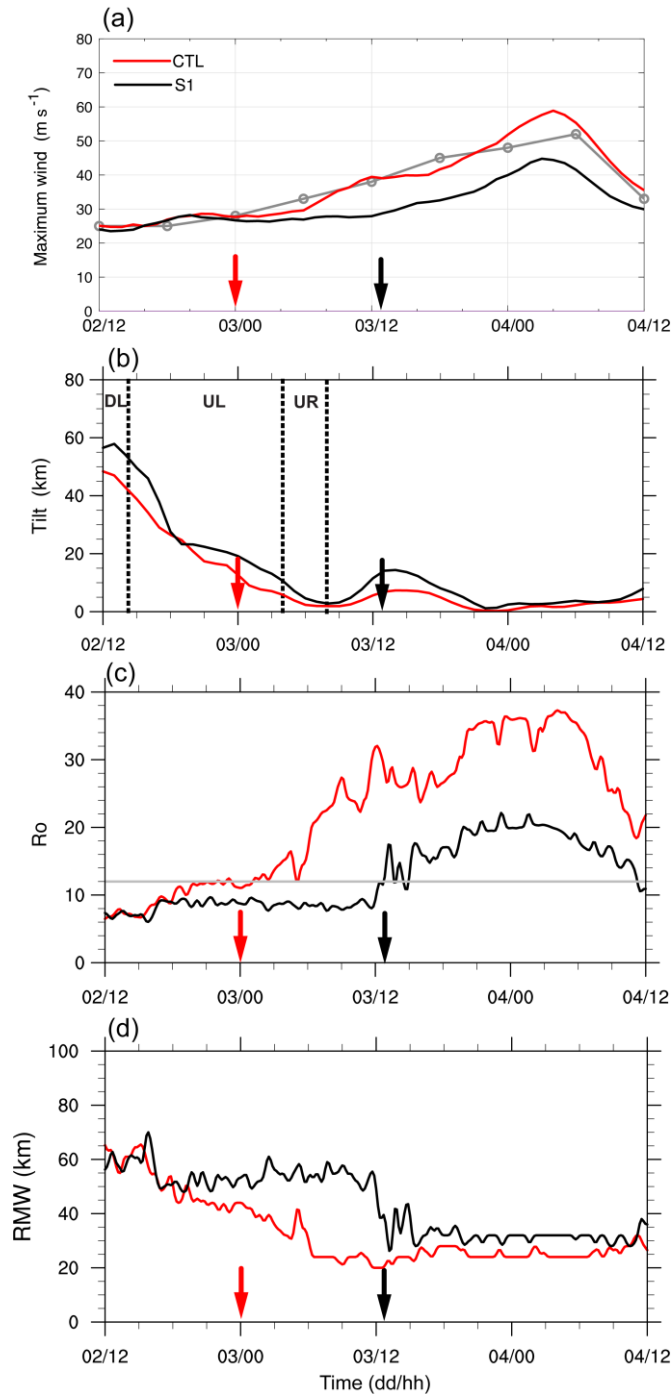
820 Fig. 11. The evolution of (a) parcel height (km) and (b) vertical velocity (m s^{-1}) along the 4-h
821 trajectory for the top 20% of the parcels that are stratified by their maximum height of the
822 4-h trajectory. The red and gray lines denote the trajectories in CTL and S1, respectively.

823 Fig. 12. Statistics for the top 20% of the parcels stratified by their maximum height of the 4-h
824 trajectory. (a) Mean parcels height during $t = 0\text{-}2 \text{ h}$ and differences in the mean θ_e from $t =$
825 0 h to $t = 2 \text{ h}$ in CTL (red) and S1 (gray). (b) Differences in the mean θ_e between CTL and
826 S1 (CTL-S1) at $t = 0 \text{ h}$ and $t = 2 \text{ h}$.

827 Fig. 13. Plan view of the (a) a_i (dynamic acceleration) + a_b (buoyancy acceleration) (shading,
828 $\times 10^{-3} \text{ m s}^{-2}$), (b) a_i , and (c) a_b averaged in the lowest 1.5 km layer and over $t = 0\text{-}2 \text{ h}$ in
829 CTL. Contours denote 1.5-km vertical velocity with values of $-1, -0.5, -0.2, 0.5, 1.0, 1.5,$
830 and 2.0 m s^{-1} (negative values dashed) averaged over the same period. (d)-(f) As in (a)-(c)
831 but in S1. The $0\text{-}2 \text{ h}$ storm-relative trajectories of the top 20% of the parcels that are
832 stratified by their maximum height of the 4-h trajectory are overlaid. The black arrow in the
833 upper-right corner denotes the heading direction of the $200\text{-}850 \text{ hPa}$ VWS. The red crosses
834 in each panel denote the starting points of these trajectories.

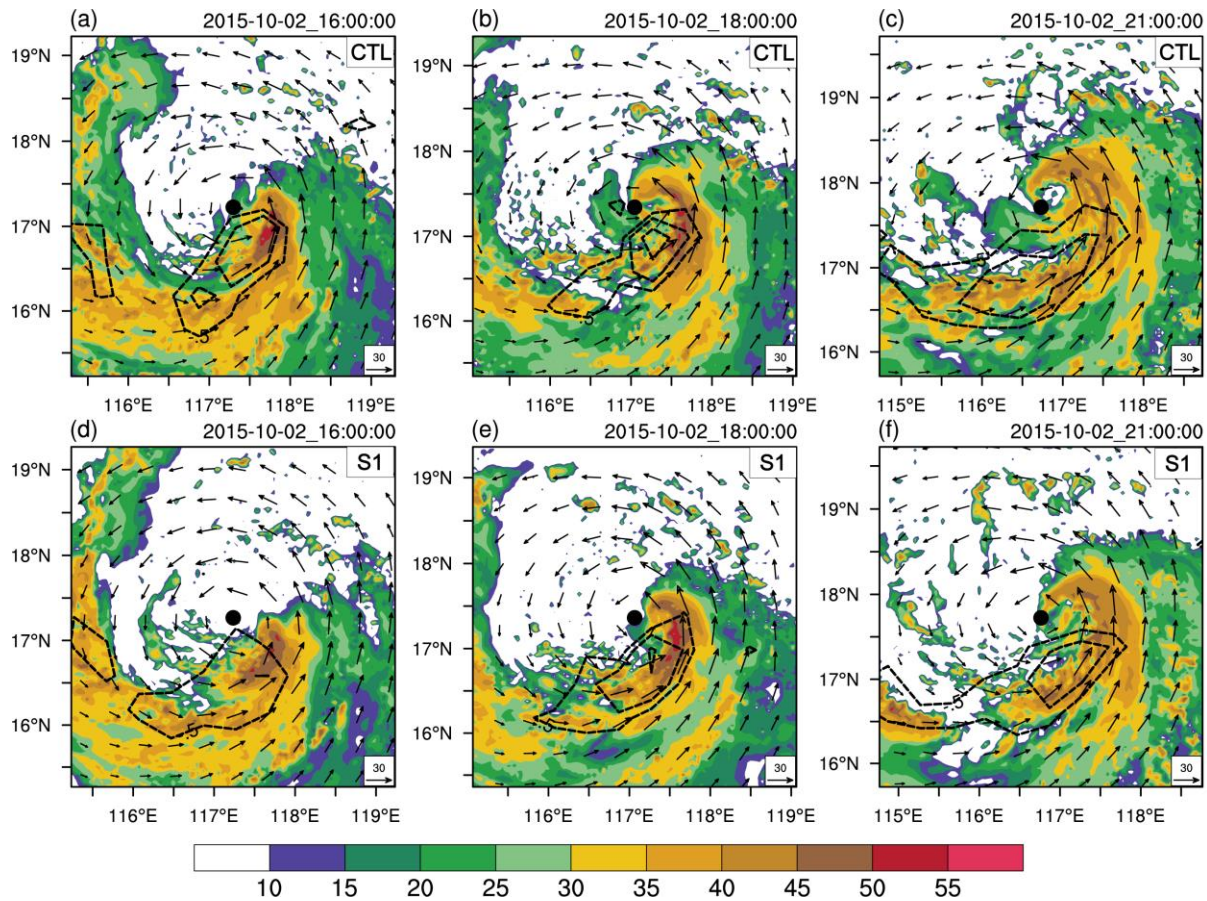
835 Fig. 14. Vertical velocity budget terms a_i , a_b , and $a_i + a_b$ (shading, $\times 10^{-3} \text{ m s}^{-2}$) averaged over
836 (a) $t = 0\text{-}2 \text{ h}$ and (b) $t = 2\text{-}3 \text{ h}$ for the top 20% of the parcels that are stratified by their
837 maximum height of the 4-h trajectory.

838 Fig. 15. As in Fig. 13, but for the results over $t=2-3$ h.
839 Fig. 16. Evolution of vertical velocity budget terms a_i (blue), a_b (red), and $a_i + a_b$ (black) over t
840 $= 2-3$ h for the top 20% of the parcels that are stratified by their maximum height of the 4-h
841 trajectory in (a) CTL and (b) S1. Lines represent mean values; shading extends from
842 minimum to maximum at each minute. The unit of the budget terms is 10^{-3} m s^{-2} .
843 Fig. 17. Azimuthal-height plot of radar reflectivity (shading, dBZ) and vertical velocity (contours
844 with values of -0.4 , -0.2 , -0.1 , 0.2 , 0.5 , 1.0 , and 2.0 m s^{-1} , negative values dashed)
845 averaged within $r = 20-60$ km and over 1800-1850 UTC 2 October for the (a) CTL and (b)
846 S1 TCs. (c)-(d) As in (a)-(b), but shading denotes relative humidity (%). The vertical dashed
847 white line marks the shear-relative quadrants, as labeled at the top of each panel. DR, UR,
848 UL, and DL denote downshear-right, upshear-right, upshear-left and downshear-left
849 quadrant, respectively.
850 Fig. 18. Conceptual model for the inward rebuilding and precipitation symmetrization under
851 different SSTs. (a) Plan view of the CPS that propagates into the upshear-left (UL)
852 quadrant. Beneath the CPS, downdraft-cooled parcels in the boundary layer subsequently
853 undergo boundary layer recovery and develop into convection during their propagation
854 toward the downshear quadrants. (b)-(c) As in (a), but at a later time before the RI onset of
855 the CTL TC over warm SSTs. In (b), the more efficient boundary layer recovery and more
856 notable inward building of deep convection in UL maintain the precipitation symmetrization
857 over warm SSTs; the stratiform in the right-of-shear semicircle in (b) indicates a nearly-
858 saturated layer above the freezing level. (c) Over relatively cool SSTs, newly-developed
859 convection in the inward rebuilding events is much weaker, which hinders precipitation
860 symmetrization. Reflectivity contours represent the CPS and convective cells. The red
861 dashed arrow in (a)-(c) denotes the trajectory along which boundary layer recovery and the
862 subsequent inward rebuilding occur. (d)-(e) Composite vertical cross-sections of reflectivity
863 and streamlines over warm and relatively cool SSTs, respectively. Locations of the cross
864 sections are marked as thick black lines in (b)-(c).
865
866



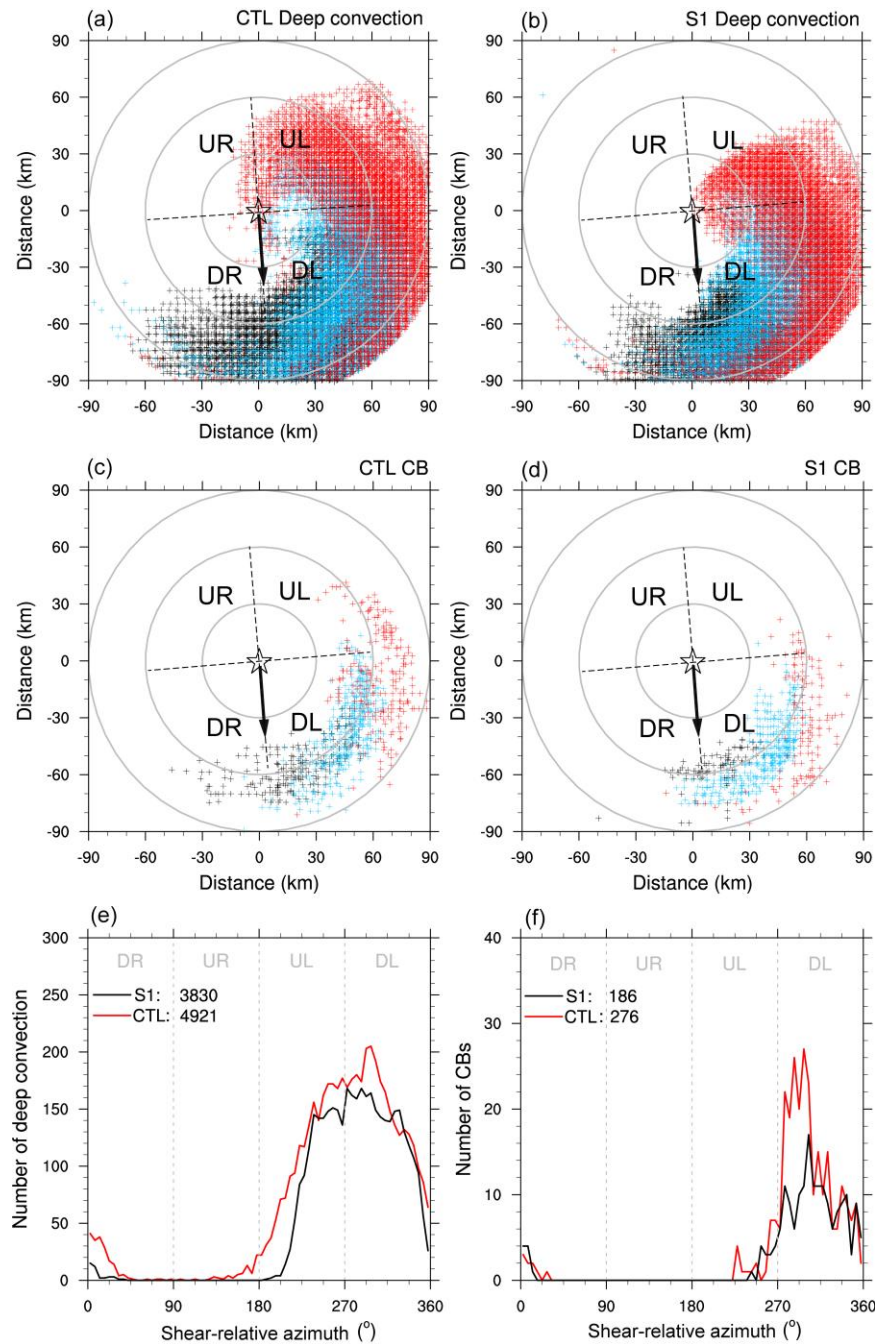
867

868 Fig. 1. Verification of simulated 10-m maximum wind speed (m s^{-1}) in the CTL (red) and S1
 869 (black) experiments against the best track data of China Meteorological Administration (gray line
 870 with circles). (b) Evolution of the 450-850 hPa vortex tilt magnitude (km) for the CTL and S1
 871 TCs from 1200 UTC 2 October to 1200 UTC 4 October. The three dashed lines mark the
 872 downshear-left (DL), upshear-left (UL), and upshear-right (UR) quadrants that the tilt vector
 873 points toward. Evolution of (c) local Rossby number R_o and (d) RMW (km) at 10-m height for
 874 the CTL and S1 TCs. The gray line in (c) denotes $R_o = 12$. The red (black) arrows in each panel
 875 denote the RI onset timing of CTL (S1) TC. Adapted from Chen et al. (2018a).



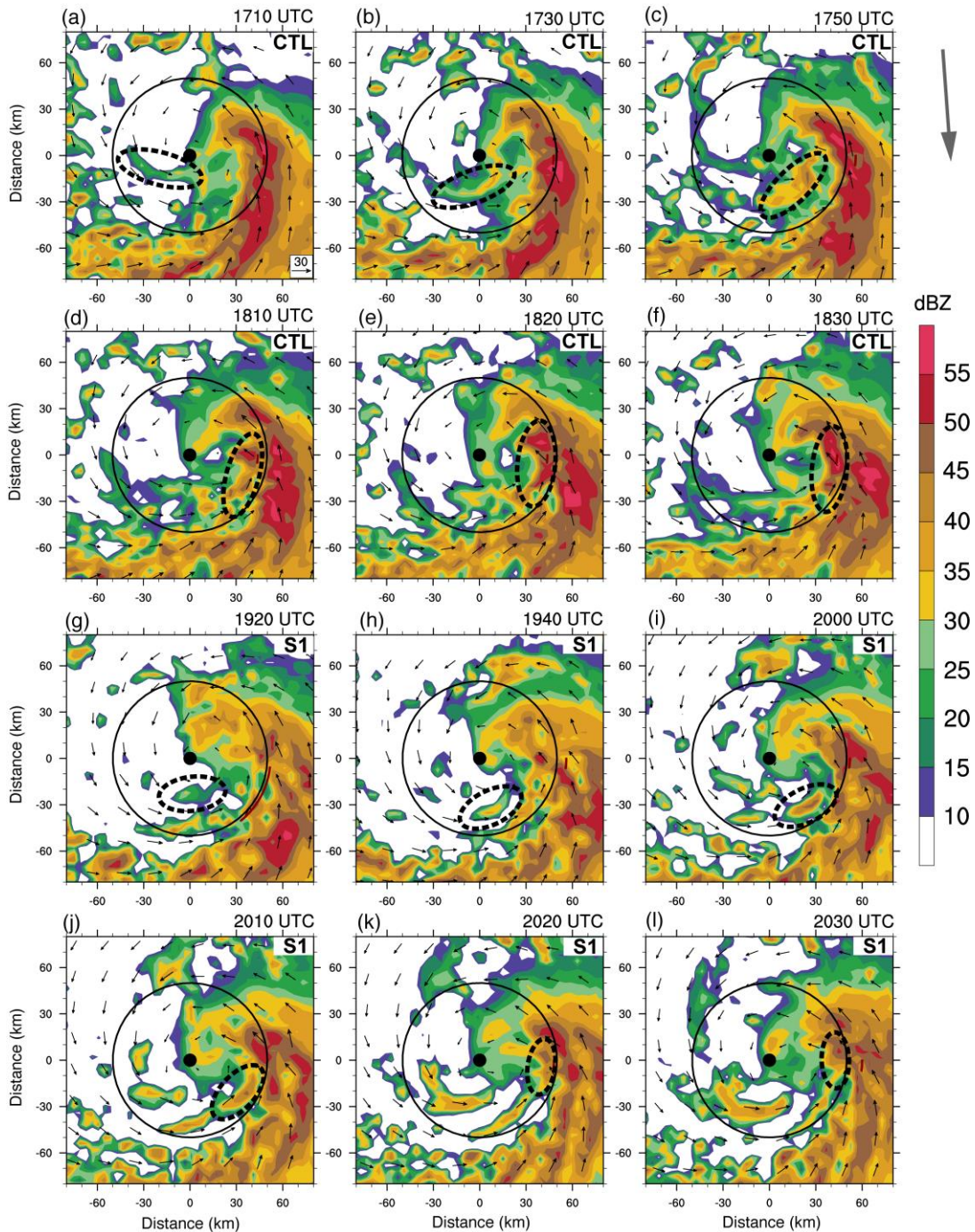
877

878 Fig. 2. (a)-(c) The 1.5-km radar reflectivity (shading; dBZ), background horizontal convergence
 879 (dashed contours with values of -2.0 , -1.0 , $-0.5 \times 10^{-4} \text{ s}^{-1}$), and storm-relative winds (vector, m s^{-1})
 880 at (a) 1600 UTC 2 October, (b) 1800 UTC 2 October, and (c) 2100 UTC 2 October in CTL.
 881 (d)-(f) As in (a)-(c), but for S1.



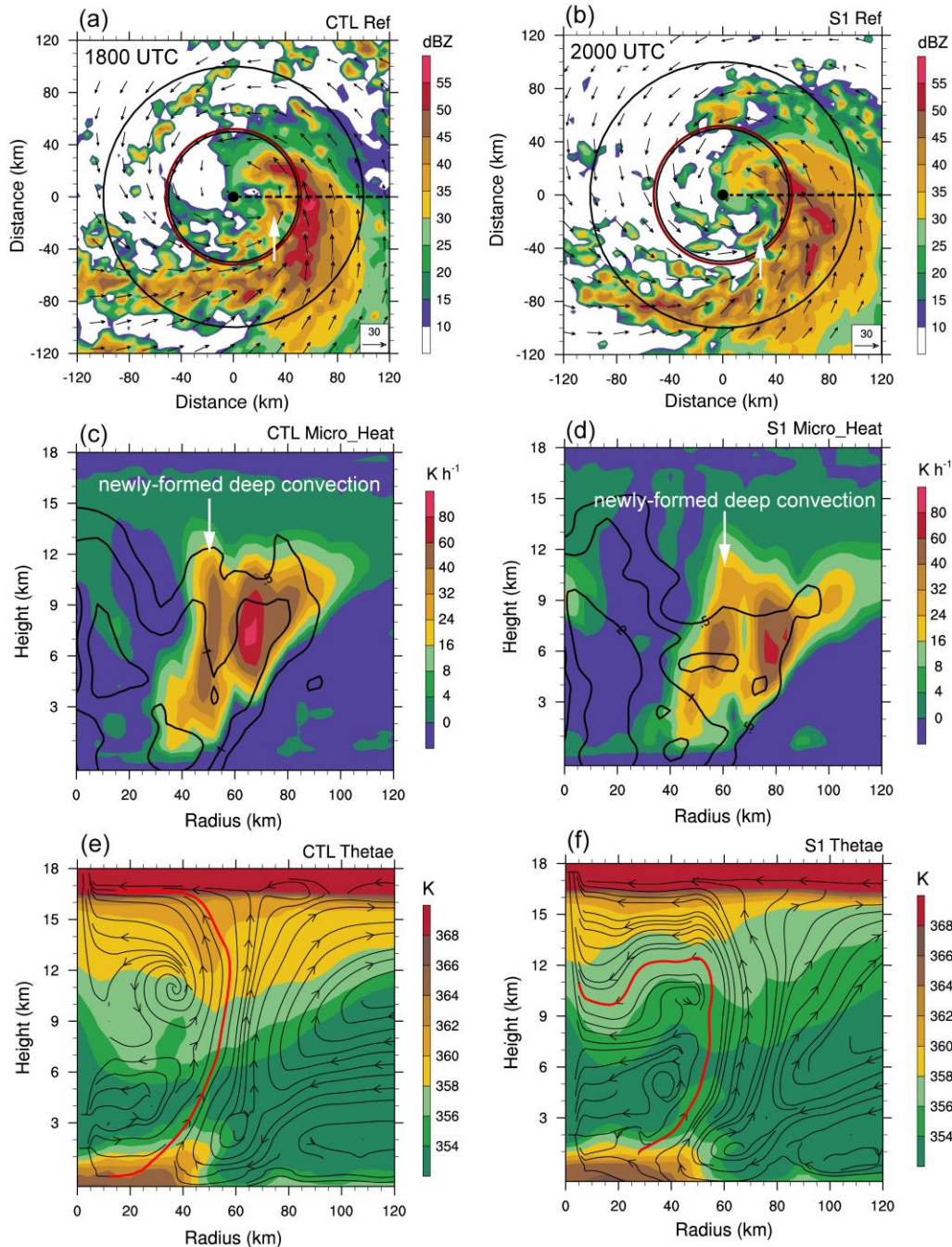
882

883 Fig. 3. (a)-(b) The location of deep convection within $r = 100$ km relative to the surface TC
 884 center (black star) occurred over 1200-1500 UTC 2 October (black plus), 1500-1800 UTC 2
 885 October (blue plus), and 1800-2100 UTC 2 October (red plus) in CTL and S1, respectively. (c)-
 886 (d) As in (a)-(b), but for the location of CBs. The black arrow in (a)-(d) denotes the 300-850 hPa
 887 vertical wind shear. Azimuthal distribution of the number of (e) grid points of deep convection
 888 and (f) CBs in CTL (red) and S1 (black) within $r = 60$ km accumulated over 1200-2100 UTC 2
 889 October at a 10-min interval. The total number of deep convection and CBs in CTL and S1 are
 890 shown as texts. The shear-relative quadrants are labeled in each panel. DR, UR, UL, and DL
 891 denote downshear-right, upshear-right, upshear-left and downshear-left quadrant, respectively.



892

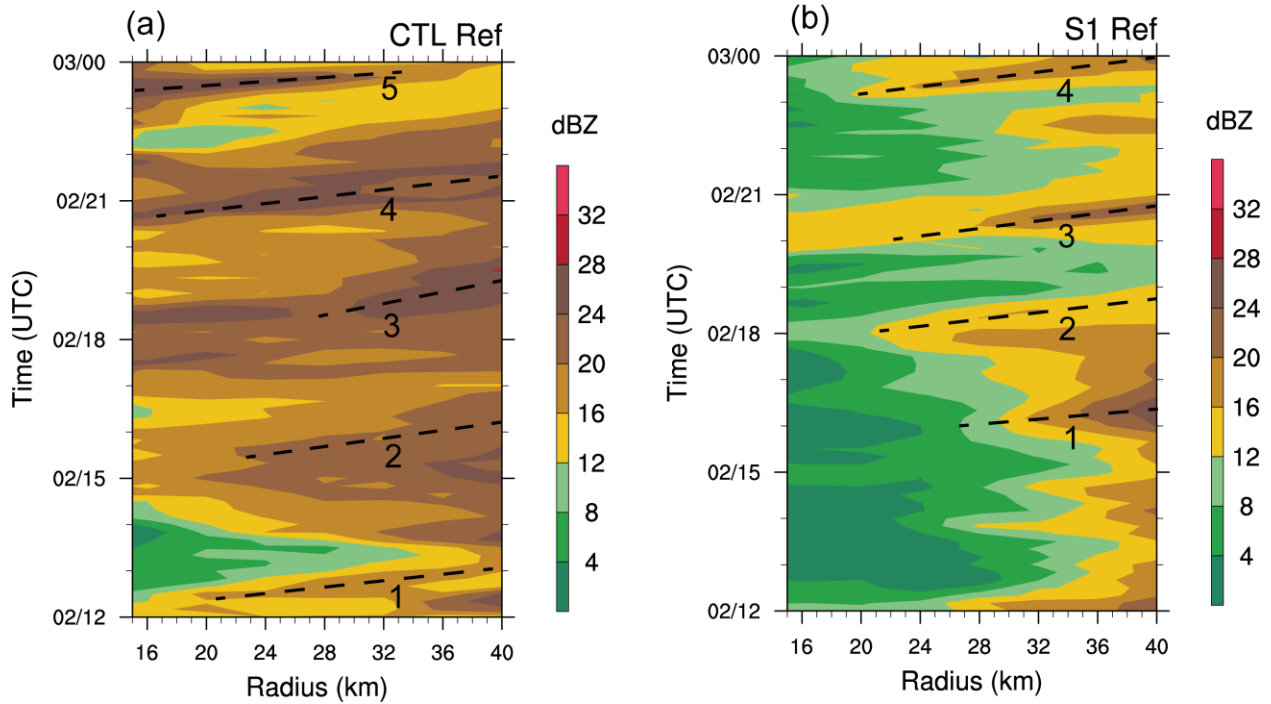
893 Fig. 4. (a)-(f) Evolution of radar reflectivity (shading, dBZ) and storm-relative wind (vector, m s^{-1})
 894 1) at the lowest model level for the CTL TC from 1710 UTC 2 October to 1830 UTC 2 October.
 895 (g)-(l) As in (a)-(f), but for the S1 TC from 1920 UTC 2 October to 2030 UTC 4 October. The
 896 solid black circle denotes the 50-km reference radius. The dashed black ellipse tracks the
 897 propagation of the developing convection inside of the RMW. The reference vector is shown in
 898 (a). The gray arrow on the top right corner denotes the heading of 200-850 hPa VWS.
 899



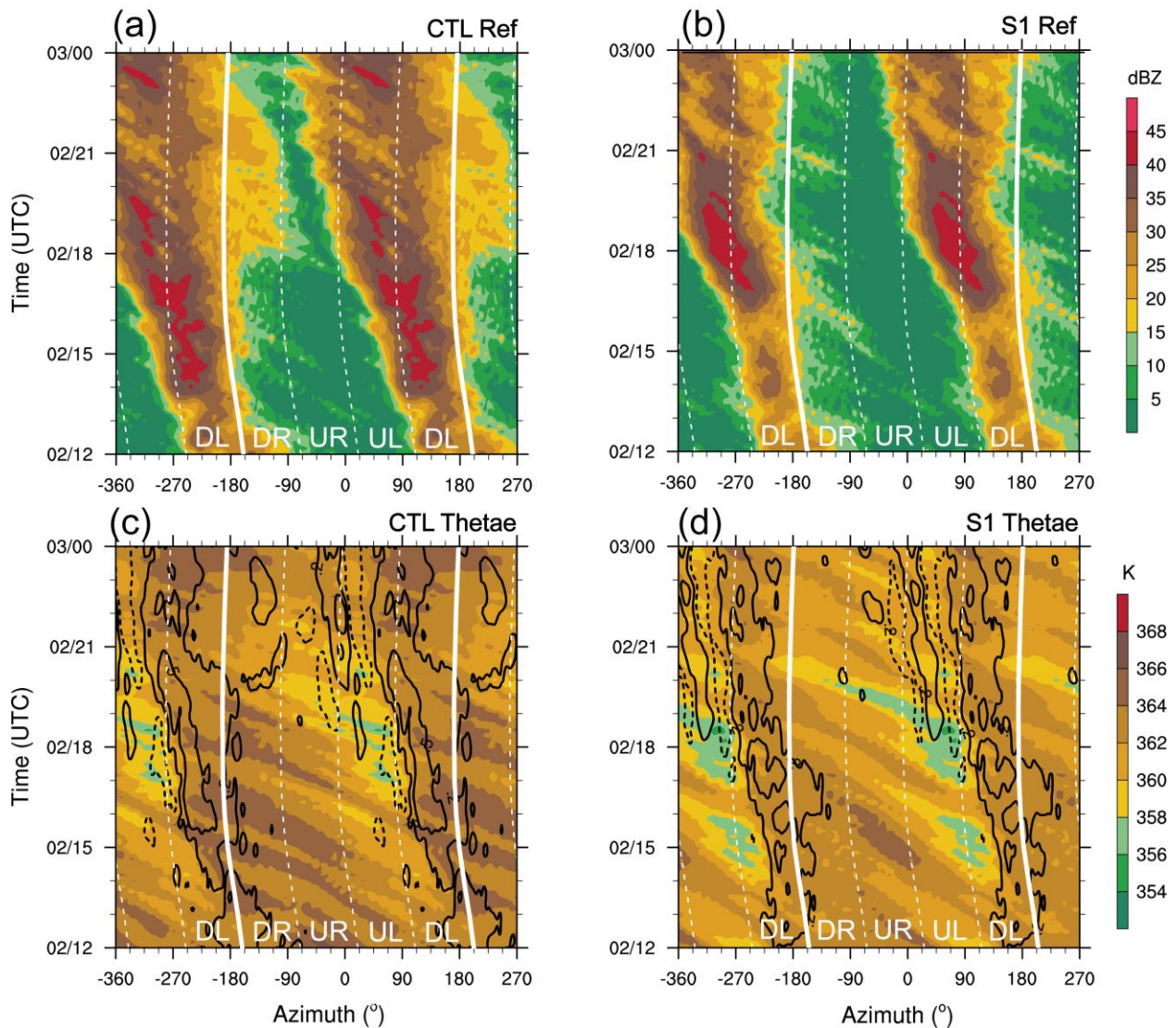
900

901 Fig. 5. (a)-(b) Plan view of radar reflectivity (shading, dBZ) and storm-relative wind (vector, m
 902 s⁻¹) at the lowest model level at 1800 UTC 2 October for the CTL and at 2000 UTC 2 October
 903 for the S1 TC, respectively. (c)-(d) Composite vertical slice of microphysics diabatic heating
 904 (shading, K h⁻¹) and absolute vorticity (contoured at 0.5, 1, and 2 × 10⁻³ s⁻¹) over 1800-1850 UTC
 905 2 October and over 2000-2050 UTC 2 October for the CTL and S1 TCs, respectively; (e)-(f) As
 906 in (c)-(d), but for θ_e (shading, K) and storm-relative wind (streamline). The position of the
 907 vertical slice in (c)-(f) is marked as black dash line in (a)-(b). The white arrow in (a)-(d) marks
 908 the location of the newly-formed deep convection. The red streamline in (e)-(f) is related to the
 909 newly-developed deep convection inside the RMW.

910

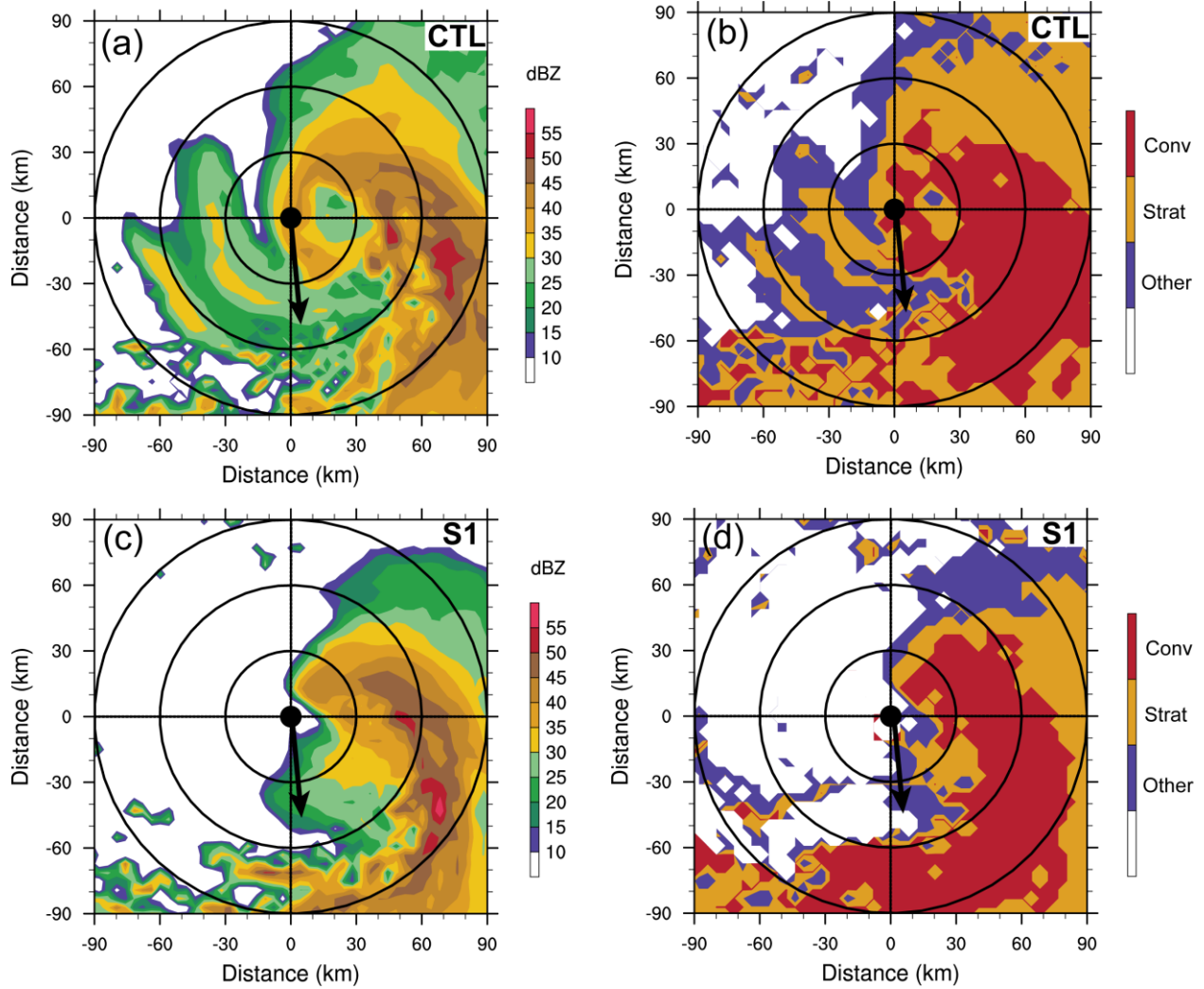


911
 912 Fig. 6. (a)-(b) Time-radius plot of radar reflectivity (shading, dBZ) averaged azimuthally within
 913 the downshear quadrants and below 500 m height from 1200 UTC 2 October to 0000 UTC 3
 914 October for the CTL and S1 TCs, respectively. The black dashed lines in each panel denote the
 915 visually trackable outward propagation of newly-formed convection within the RMW.
 916



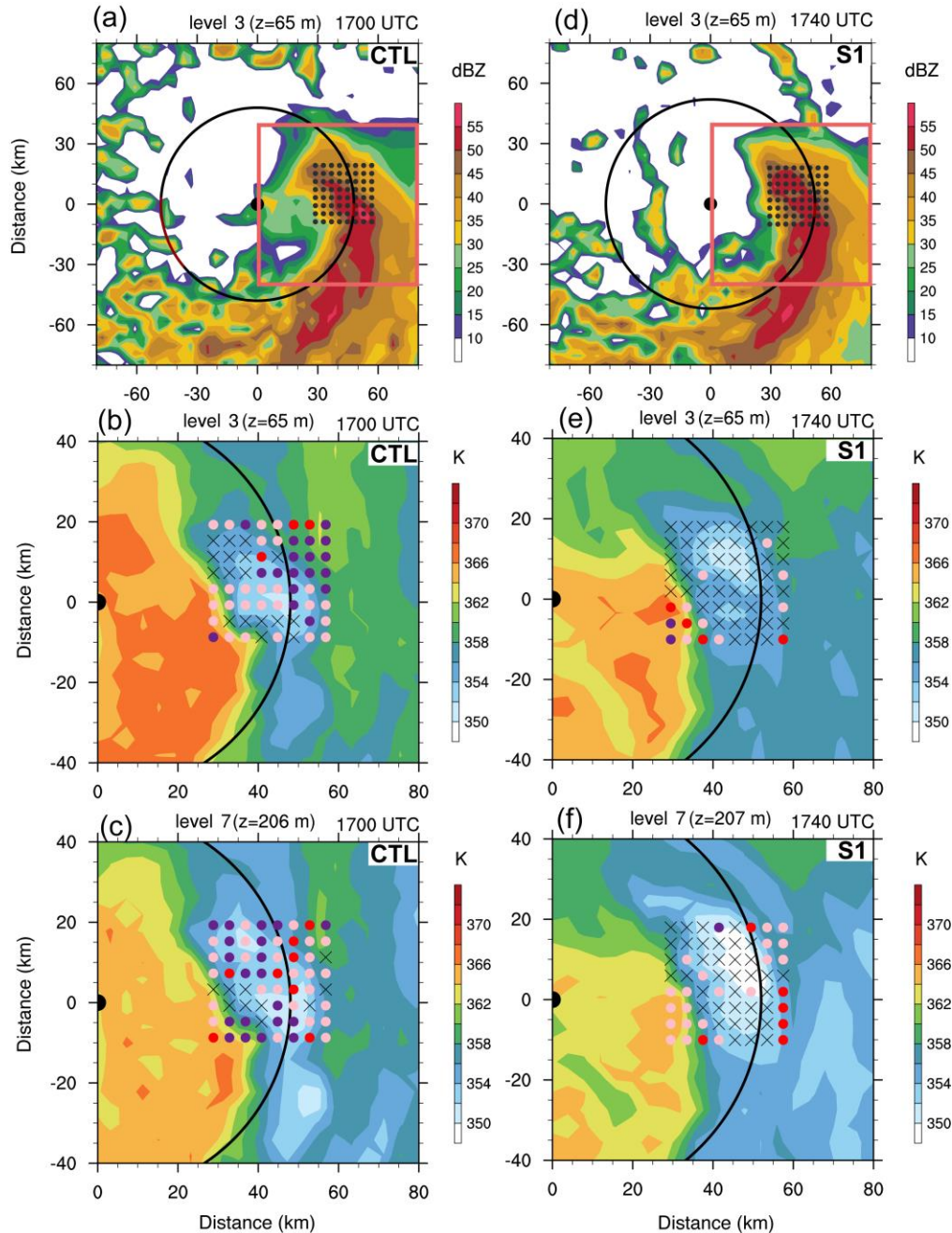
917

918 Fig. 7. (a)-(b) Time-azimuthal plot of radar reflectivity (shading, dBZ) for the CTL and S1 TCs,
 919 respectively. (c)-(d) As in (a)-(b), but for θ_e (shading, K) and vertical velocity (contours with
 920 values of -0.2 , 0.2 , and 0.5 m s^{-1} and negative values are dashed) for the two TCs. The radar
 921 reflectivity and θ_e are averaged within $r = 20\text{-}50 \text{ km}$ and below 500-m height. The vertical
 922 velocity is averaged within $r = 20\text{-}50 \text{ km}$ at 1-km height. The solid white line denotes the
 923 heading direction of $200\text{-}850 \text{ hPa}$ VWS. The dashed white line marks the shear-relative
 924 quadrants, as labeled at the bottom of each panel. DR, UR, UL, and DL denote downshear-right,
 925 upshear-right, upshear-left and downshear-left quadrant, respectively.



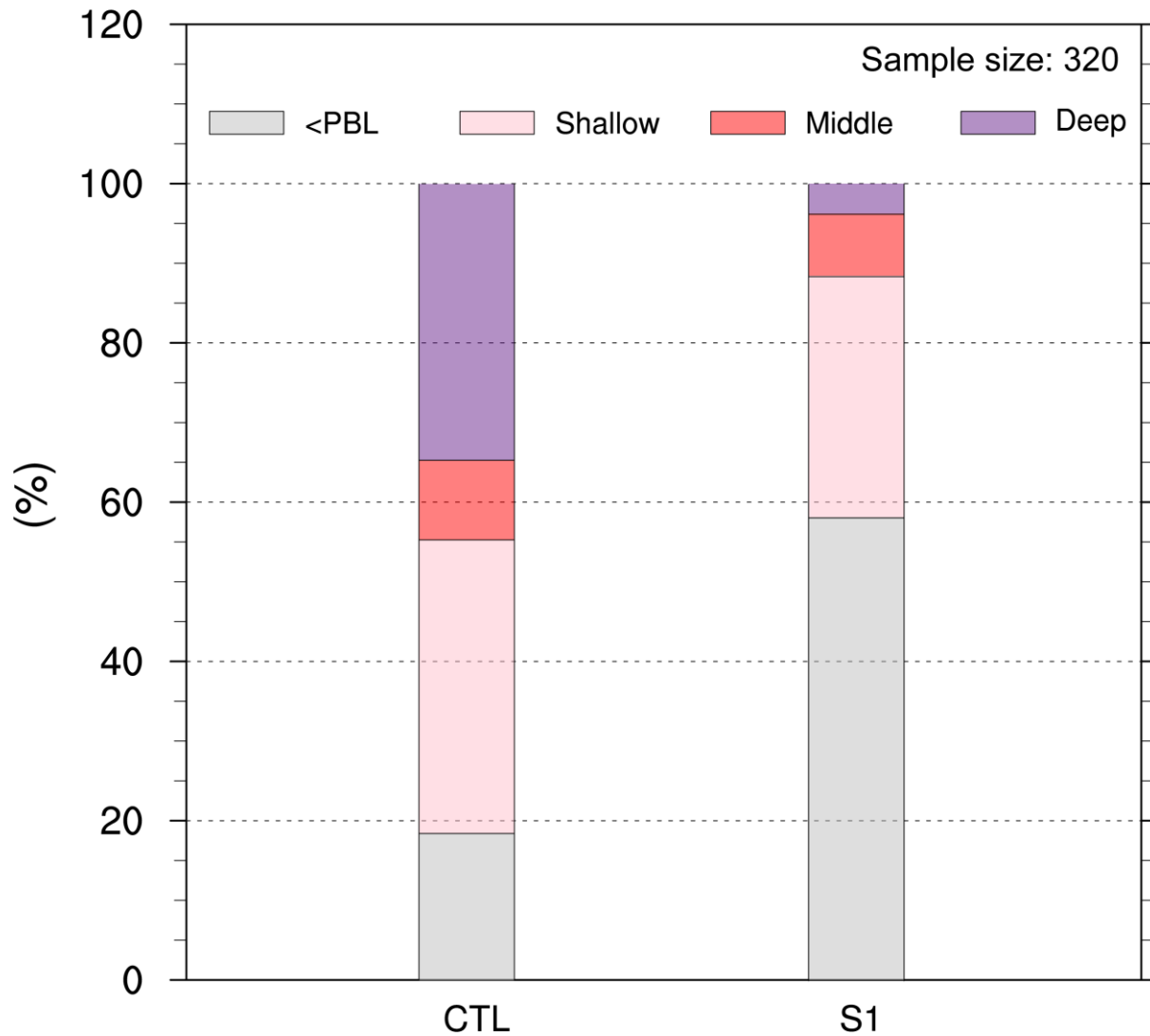
926

927 Fig. 8. Plan view of (a) radar reflectivity (shading, dBZ) at 3-km height and (b) precipitation
 928 mode at 1830 UTC 2 October. The red, yellow, and purple area in (b) denote convective,
 929 stratiform, and other type precipitation, respectively. (c)-(d) As in (a)-(b), but for S1 TC. The
 930 solid black arrow in (a)-(d) denotes the heading direction of 200-850 hPa VWS.
 931

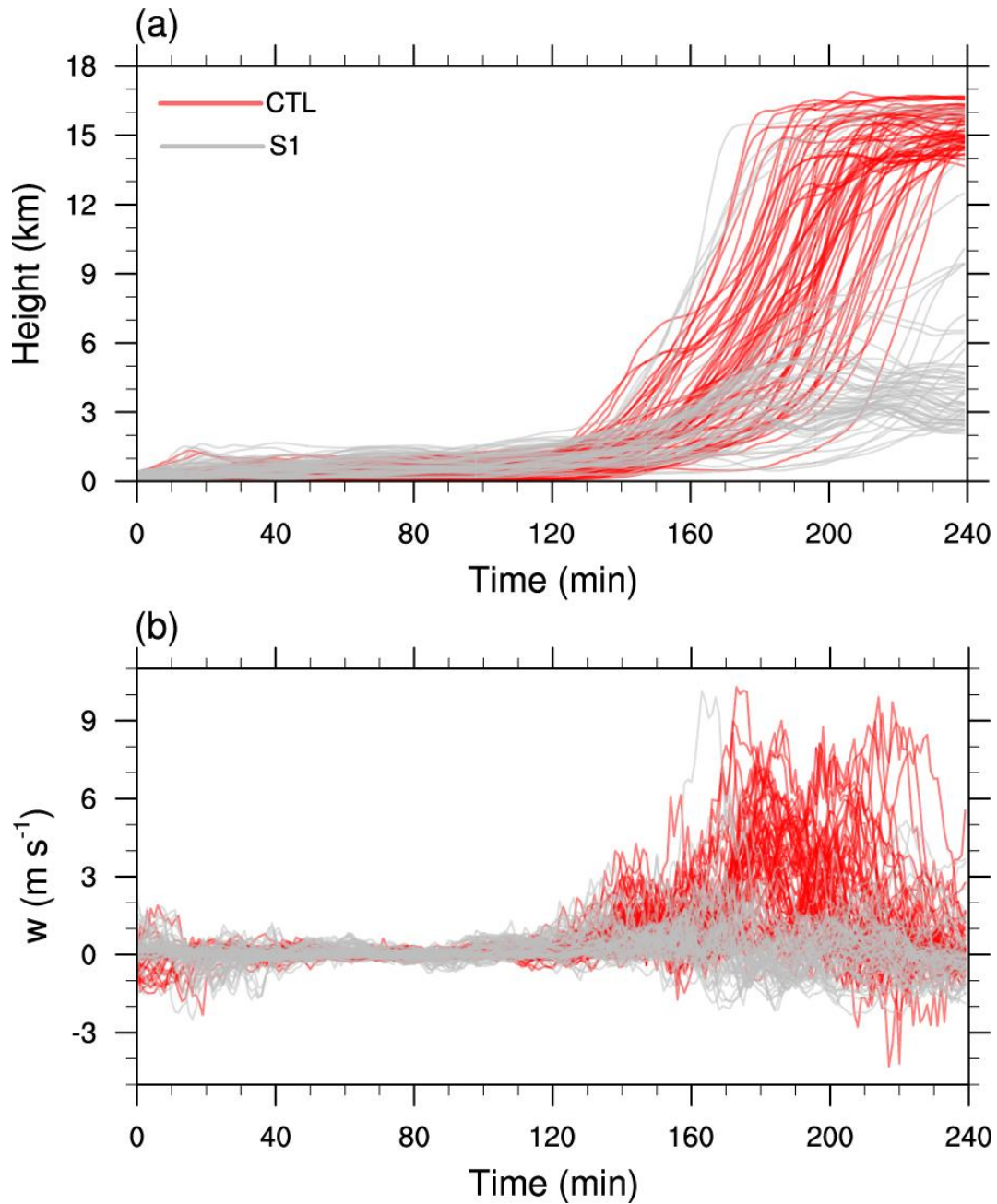


932

933 Fig. 9. Plan view of (a) radar reflectivity (shading, dBZ) at the 3rd lowest model level, θ_e
 934 (shading, K) at the (b) 3rd and (c) 7th lowest model levels at 1700 UTC 2 October for the CTL
 935 TC. (d)-(f) As in (a)-(c), but for the S1 TC at 1740 UTC. The location of the initial points of the
 936 trajectories are shown as black dots in (a) and (d), and are shown as colored dots based on the
 937 maximum height of the subsequent 4-h forward trajectory in (b)-(c) and (e)-(f). Black cross (×)
 938 denotes the boundary layer parcels with the maximum height <1.5 km. Pink, red, and violet dots
 939 denote the maximum height of these parcels within 1.5-4 km, 4-8 km, and >8 km, respectively.
 940 The large black dot at (0, 0) marks the surface TC center. The black circle represents the RMW
 941 near the surface. The orange box in (a) and (e) denotes the same area of (b)-(c) and (e)-(f),
 942 respectively. The mean height of each model level is shown in the title of each panel.

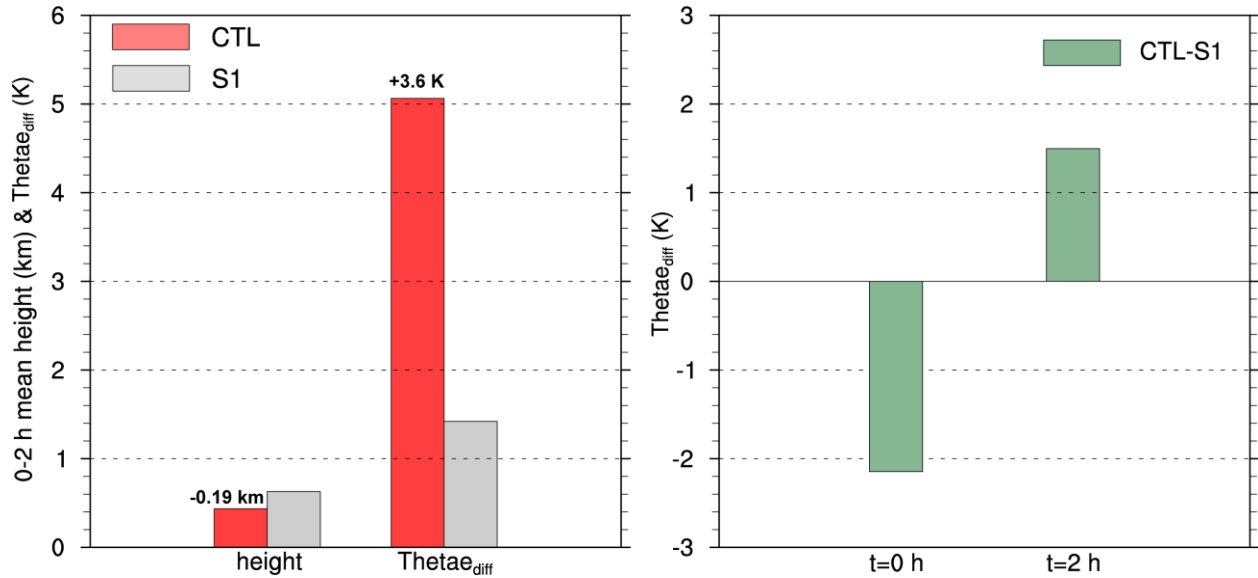


943
 944 Fig. 10. Bar plot of the ratio of the track parcels that remain in the boundary layer (gray) or
 945 develop into the shallow (pink), midlevel (red) and deep (purple) convection in the CTL and S1
 946 experiments.
 947



948

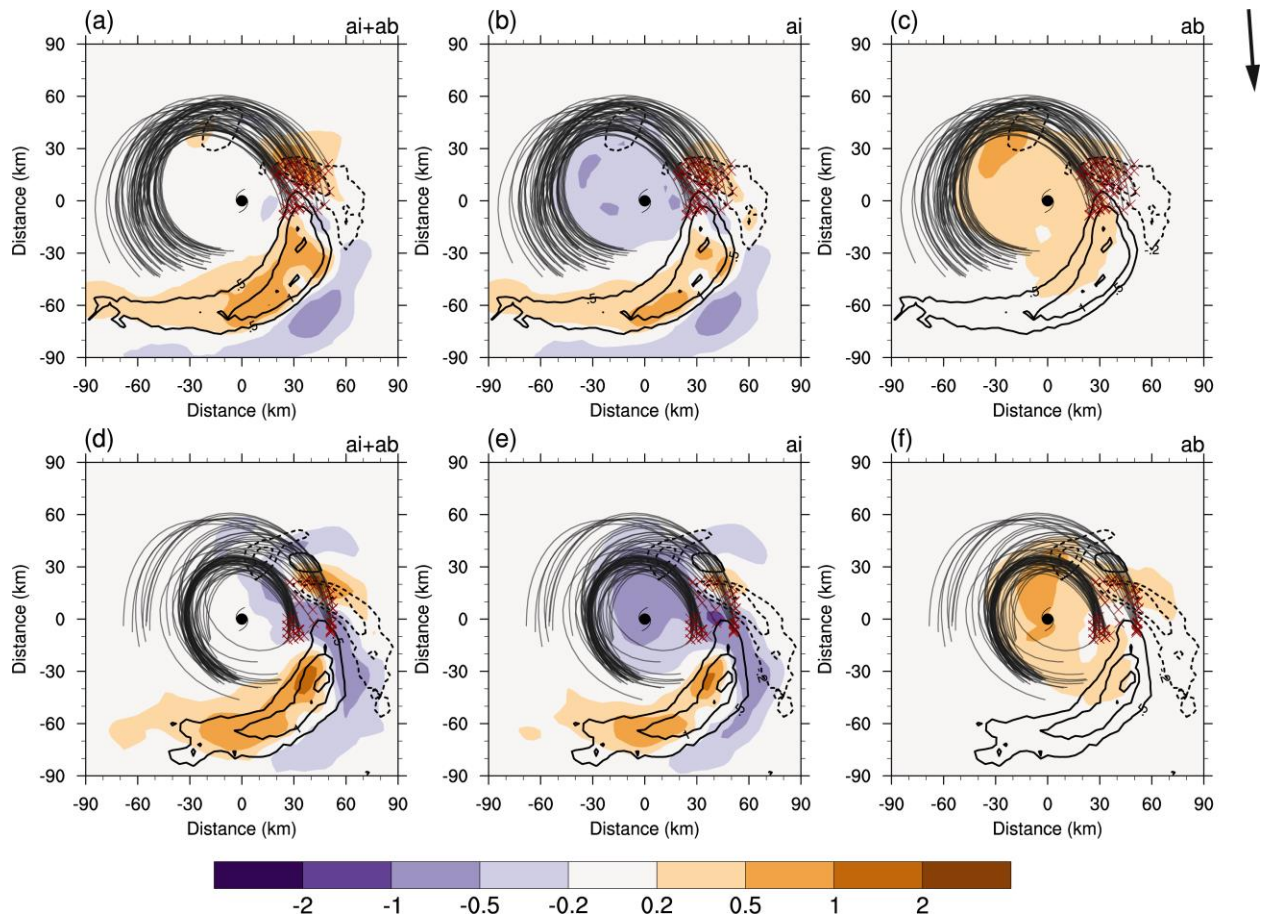
949 Fig. 11. The evolution of (a) parcel height (km) and (b) vertical velocity (m s^{-1}) along the 4-h
 950 trajectory for the top 20% of the parcels that are stratified by their maximum height of the 4-h
 951 trajectory. The red and gray lines denote the trajectories in CTL and S1, respectively.



952

953 Fig. 12. Statistics for the top 20% of the parcels stratified by their maximum height of the 4-h
 954 trajectory. (a) Mean parcels height during $t = 0-2$ h and differences in the mean θ_e from $t = 0$ h to
 955 $t = 2$ h in CTL (red) and S1 (gray). (b) Differences in the mean θ_e between CTL and S1 (CTL–
 956 S1) at $t = 0$ h and $t = 2$ h.

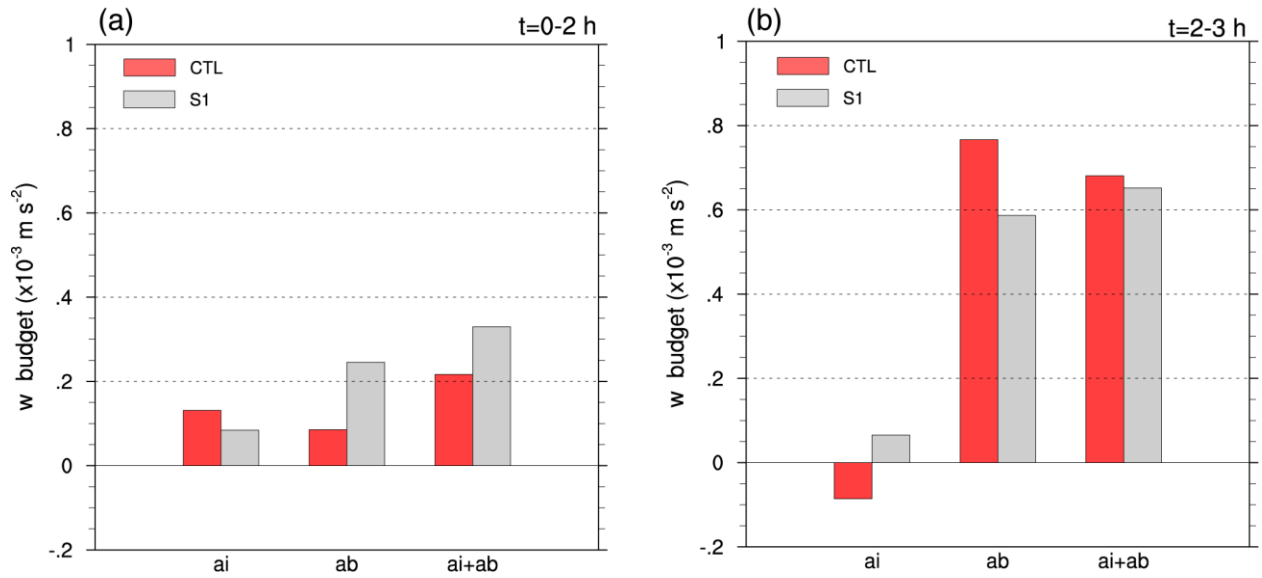
957



958

959 Fig. 13. Plan view of the (a) a_i (dynamic acceleration) + a_b (buoyancy acceleration) (shading,
 960 $\times 10^{-3} \text{ m s}^{-2}$), (b) a_i , and (c) a_b averaged in the lowest 1.5 km layer and over $t = 0-2 \text{ h}$ in CTL.
 961 Contours denote 1.5-km vertical velocity with values of $-1, -0.5, -0.2, 0.5, 1.0, 1.5,$ and 2.0 m s^{-1}
 962 $(\text{negative values dashed})$ averaged over the same period. (d)-(f) As in (a)-(c) but in S1. The 0-2
 963 h storm-relative trajectories of the top 20% of the parcels that are stratified by their maximum
 964 height of the 4-h trajectory are overlaid. The black arrow in the upper-right corner denotes the
 965 heading direction of the 200-850 hPa VWS. The red crosses in each panel denote the starting
 966 points of these trajectories.

967



968

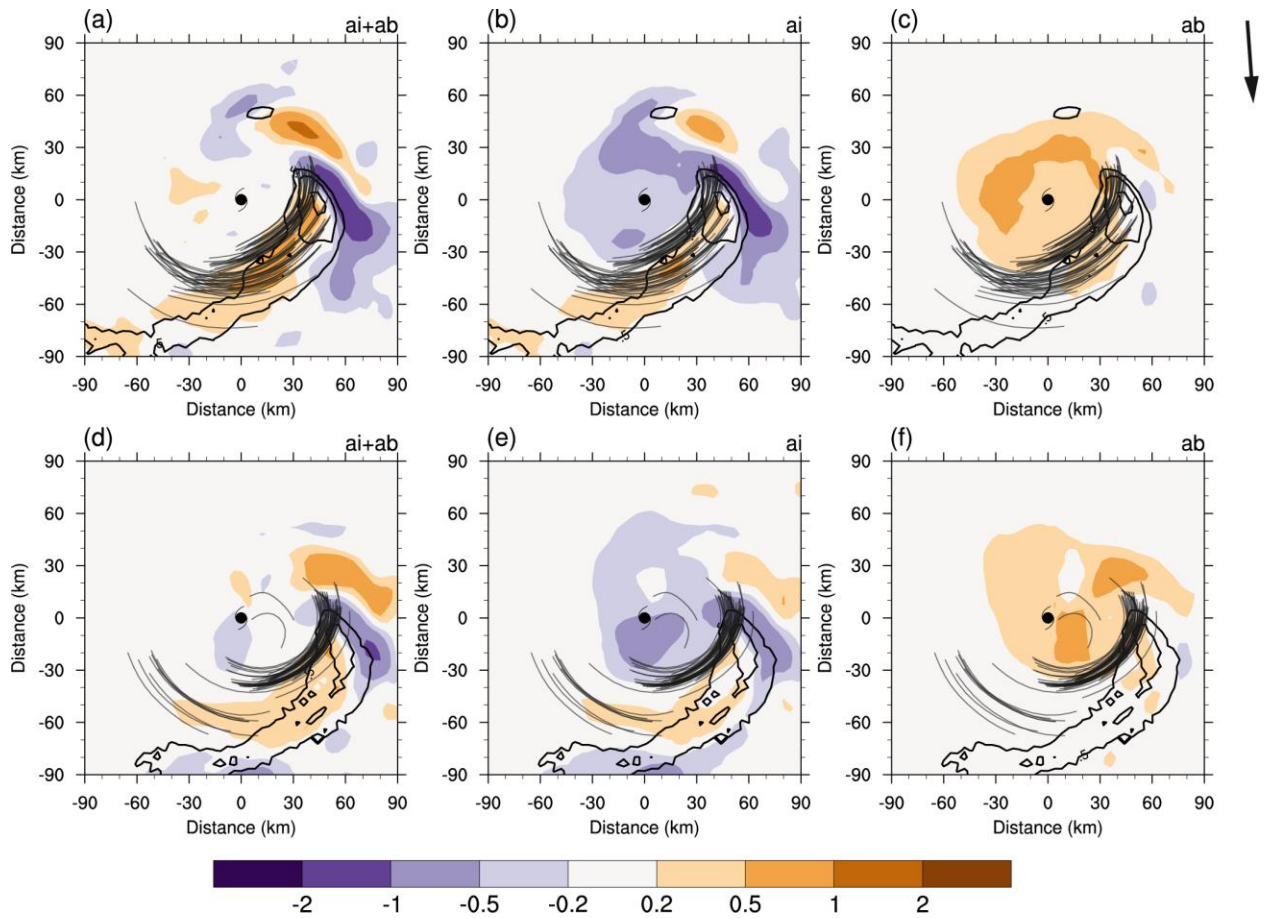
969

970

971

972

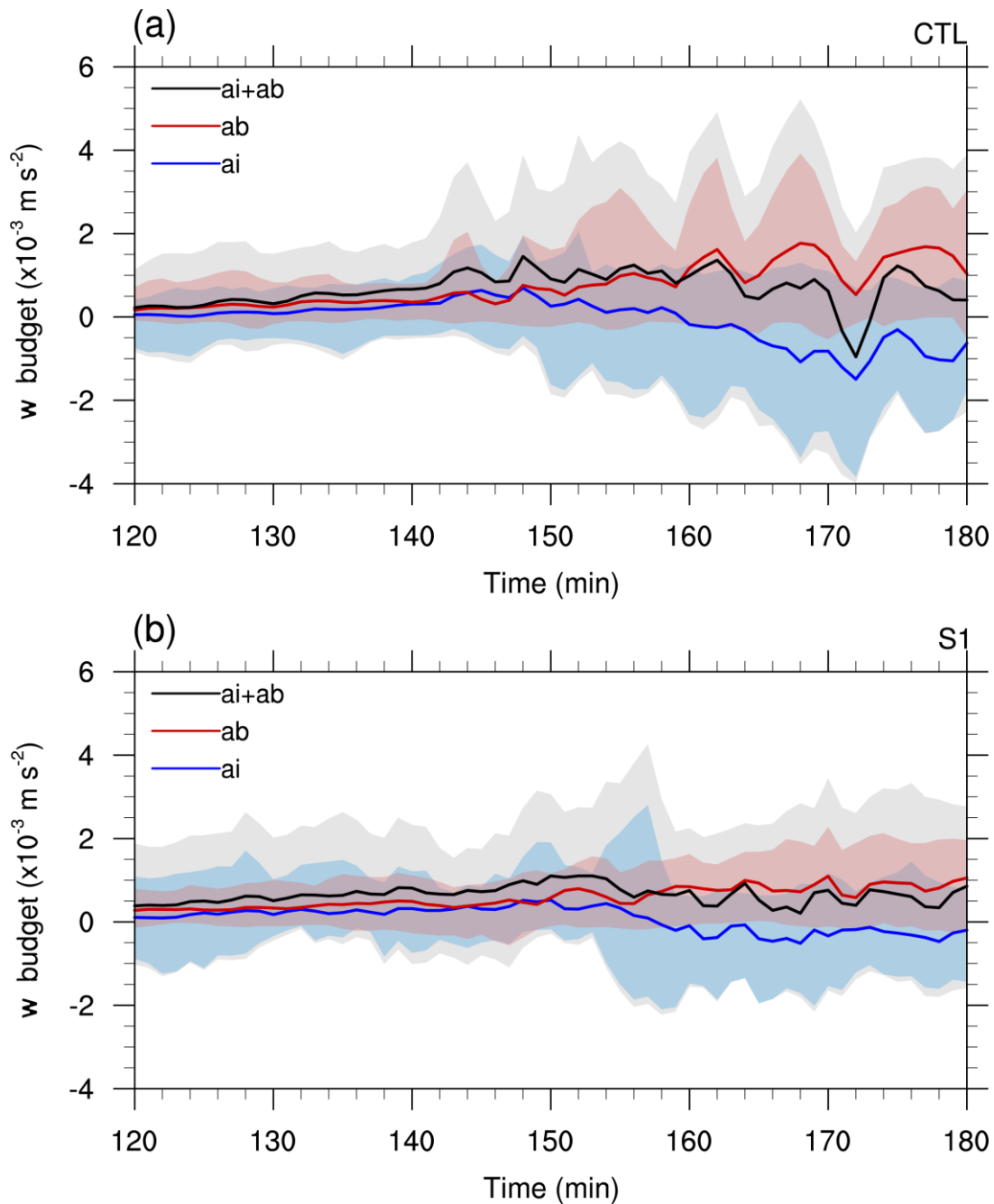
Fig. 14. Vertical velocity budget terms a_i , a_b , and $a_i + a_b$ (shading, $\times 10^{-3} \text{ m s}^{-2}$) averaged over the top 20% of the parcels that are stratified by their maximum height of the 4-h trajectory.



973

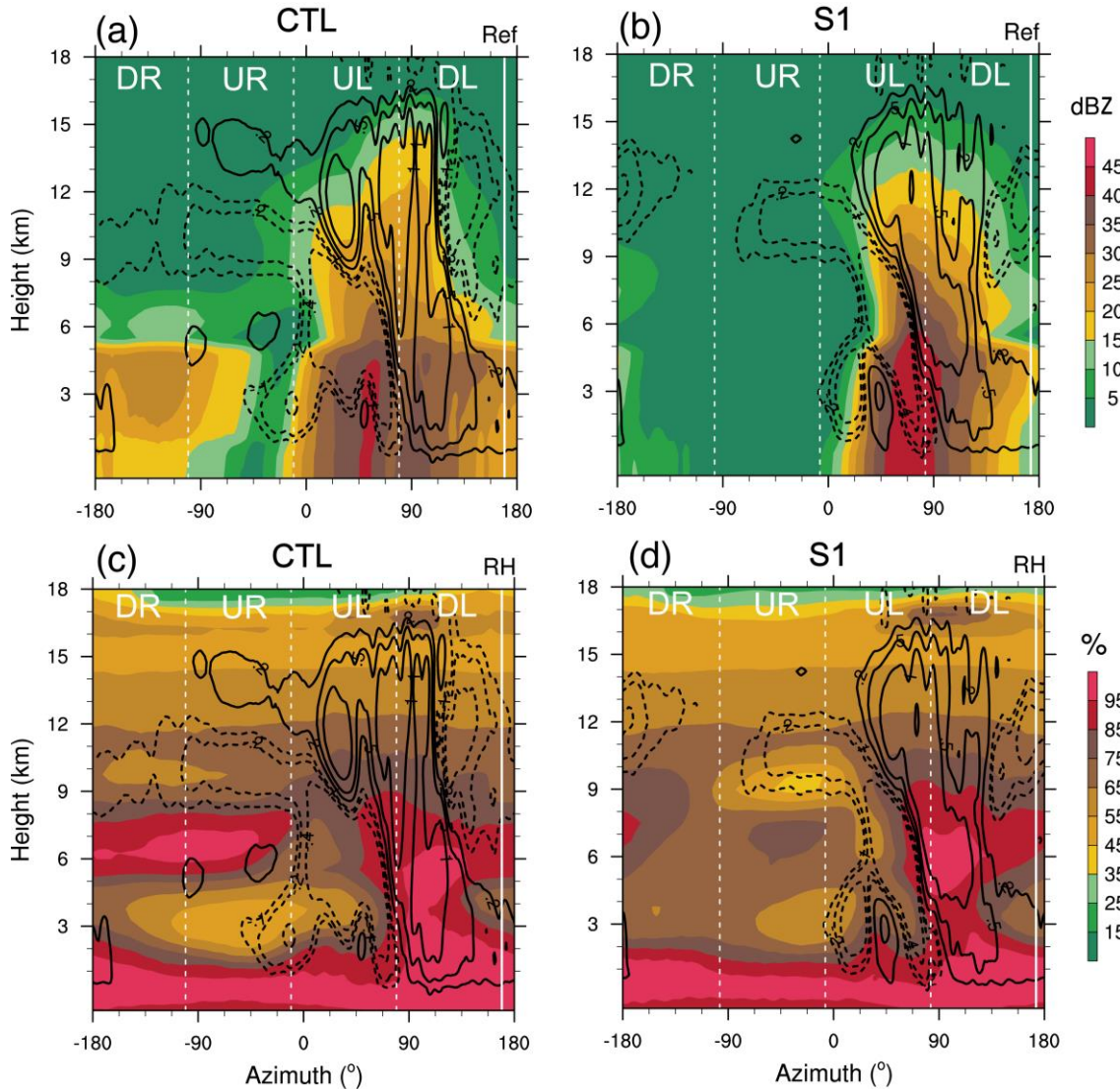
974 Fig. 15. As in Fig. 13, but for the results over $t=2-3$ h.

975



976

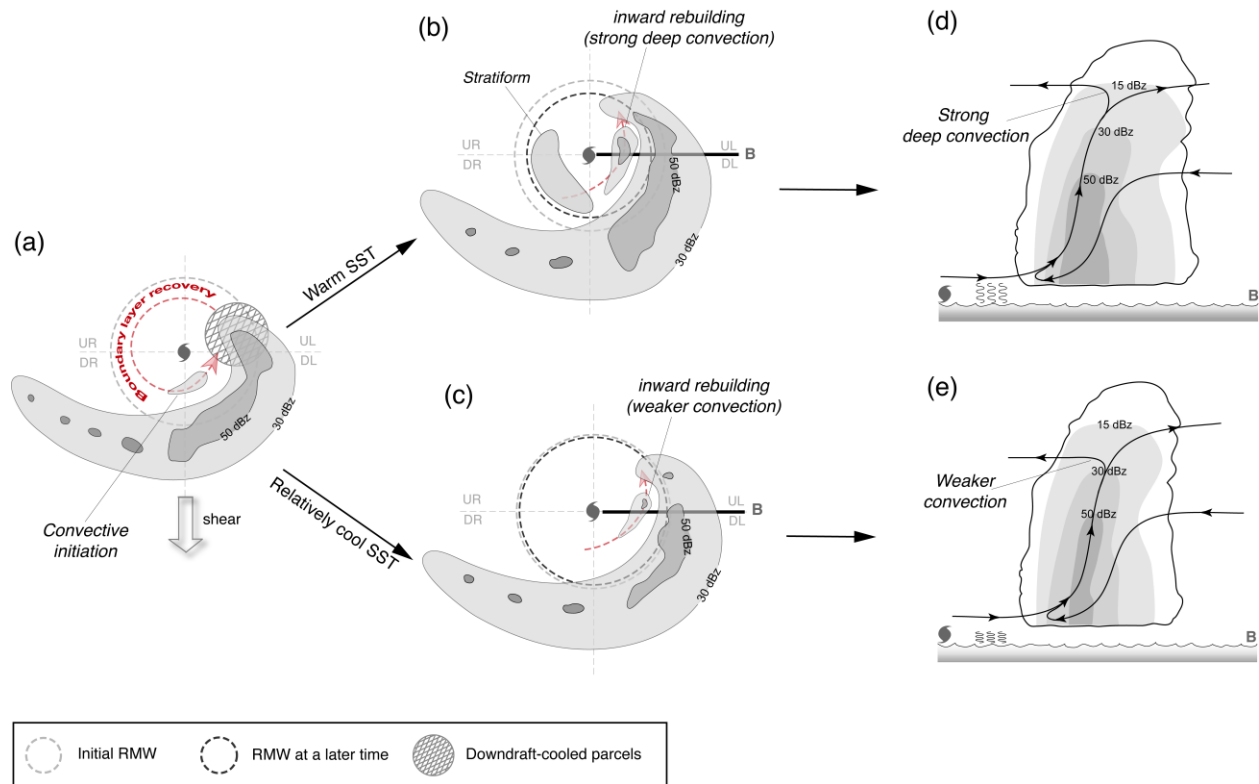
977 Fig. 16. Evolution of vertical velocity budget terms a_i (blue), a_b (red), and $a_i + a_b$ (black) over t
 978 $= 2\text{-}3$ h for the top 20% of the parcels that are stratified by their maximum height of the 4-h
 979 trajectory in (a) CTL and (b) S1. Lines represent mean values; shading extends from minimum to
 980 maximum at each minute. The unit of the budget terms is 10^{-3} m s^{-2} .
 981



982

983 Fig. 17. Azimuthal-height plot of radar reflectivity (shading, dBZ) and vertical velocity (contours
 984 with values of -0.4 , -0.2 , -0.1 , 0.2 , 0.5 , 1.0 , and 2.0 m s^{-1} , negative values dashed) averaged
 985 within $r = 20\text{-}60$ km and over 1800-1850 UTC 2 October for the (a) CTL and (b) S1 TCs. (c)-(d)
 986 As in (a)-(b), but shading denotes relative humidity (%). The vertical dashed white line marks the
 987 shear-relative quadrants, as labeled at the top of each panel. DR, UR, UL, and DL denote
 988 downshear-right, upshear-right, upshear-left and downshear-left quadrant, respectively.

989



990

991 Fig. 18. Conceptual model for the inward rebuilding and precipitation symmetrization under
 992 different SSTs. (a) Plan view of the CPS that propagates into the upshear-left (UL) quadrant.
 993 Beneath the CPS, downdraft-cooled parcels in the boundary layer subsequently undergo
 994 boundary layer recovery and develop into convection during their propagation toward the
 995 downshear quadrants. (b)-(c) As in (a), but at a later time before the RI onset of the CTL TC over
 996 warm SSTs. In (b), the more efficient boundary layer recovery and more notable inward building
 997 of deep convection in UL maintain the precipitation symmetrization over warm SSTs; the
 998 stratiform in the right-of-shear semicircle in (b) indicates a nearly-saturated layer above the
 999 freezing level. (c) Over relatively cool SSTs, newly-developed convection in the inward
 1000 rebuilding events is much weaker, which hinders precipitation symmetrization. Reflectivity
 1001 contours represent the CPS and convective cells. The red dashed arrow in (a)-(c) denotes the
 1002 trajectory along which boundary layer recovery and the subsequent inward rebuilding occur. (d)-
 1003 (e) Composite vertical cross-sections of reflectivity and streamlines over warm and relatively
 1004 cool SSTs, respectively. Locations of the cross sections are marked as thick black lines in (b)-(c).
 1005